

^{171}Yb Reference Data

Ronen M. Kroeze^{1,2,*} Sofus Laguna Kristensen^{2,3,†} and Sebastian Pucher^{2,3,4,‡}

¹*Fakultät für Physik, Ludwig-Maximilians-Universität, 80799 München, Germany*

²*Munich Center for Quantum Science and Technology, 80799 München, Germany*

³*Max-Planck-Institut für Quantenoptik, 85748 Garching, Germany*

⁴*Atom Computing, Inc., 2500 55th St, Boulder, Colorado 80301, USA*

(Dated: February 16, 2026)

Ytterbium-171 is a versatile atomic species often used in quantum optics, precision metrology, and quantum computing. Consolidated atomic data is essential for the planning, execution, and evaluation of experiments. In this reference, we present physical and optical properties of neutral ^{171}Yb relevant to these applications. We emphasize experimental results and supplement these with theoretical estimates. We present equations to convert values and derive important parameters. Tabulated results include key parameters for commonly used transitions in ^{171}Yb ($^1\text{S}_0 \rightarrow ^1\text{P}_1$, $^1\text{S}_0 \rightarrow ^3\text{P}_{0,1,2}$, $^3\text{P}_{0,2} \rightarrow ^3\text{S}_1$, and $^3\text{P}_0 \rightarrow ^3\text{D}_1$). This dataset serves as an up-to-date reference for studies involving fermionic ^{171}Yb .

1. INTRODUCTION

In this reference, we present the physical and optical properties of ytterbium-171 (^{171}Yb) relevant to various quantum optics, laser cooling, and precision measurement experiments. This document is inspired by the widely used references on alkali atoms by Daniel A. Steck [1–4], and follows the structure of a similar document on ^{88}Sr [5]. Our goal is to provide experimentalists and theorists with consolidated data and calculated parameters that are important for understanding the interaction of light with ytterbium atoms.

We consider the relevant electronic level structure of ^{171}Yb , in the context of laser cooling, optical trapping, coherent manipulation, and optical clock operation. In particular, we summarize the following optical transitions:

- The broad, dipole-allowed $^1\text{S}_0 \rightarrow ^1\text{P}_1$ transition at a wavelength λ of about 399 nm, which is used for first-stage laser cooling and Zeeman slowing (blue MOT transition), but also commonly used for atomic imaging schemes.
- The narrow spin-forbidden intercombination $^1\text{S}_0 \rightarrow ^3\text{P}_1$ transition at $\lambda \approx 556$ nm, used for second-stage cooling to microkelvin temperatures (green MOT transition) and additionally for coherent control or imaging of the nuclear spin state.
- The ultra-narrow $^1\text{S}_0 \rightarrow ^3\text{P}_0$ transition at $\lambda \approx 578$ nm, used in optical lattice clocks for precision timekeeping and as an optical qubit for quantum information applications (yellow clock transition).
- The ultra-narrow $^1\text{S}_0 \rightarrow ^3\text{P}_2$ transition at $\lambda \approx 507$ nm, relevant for, e.g., quantum simulations (green clock transition).
- The additional dipole-allowed transitions at $\lambda \approx 649$ nm, 770 nm, and 1389 nm to excite atoms into the $^3\text{S}_1$ or $^3\text{D}_1$ states, primarily used to manipulate and repump population of the long-lived metastable $^3\text{P}_0$ and $^3\text{P}_2$ states back into the ground state.

Notable omissions are the $^3\text{P}_1 \rightarrow ^3\text{D}_1$ transition used for state preparation into the long-lived $^3\text{P}_{0,2}$ states, the $^3\text{P}_2 \rightarrow ^3\text{D}_3$ cycling transition that is relevant to quantum-optics applications [6], and the $^1\text{S}_0 \rightarrow 4f^{13}5d6s^2(J=2)$ transition to a core-excited state that is relevant for studying beyond-Standard Model physics [7–9]. These might be included in future updates.

Measured values are provided with their corresponding references to original experimental sources, while calculated quantities are derived using established physical models, with citations to more detailed theoretical discussions. The data provided here are not guaranteed to be complete or error-free. For parameters critical to your research, you should consult the primary literature.

This document is intended as a community resource, following the example of Steck’s *Alkali D Line Data* series, available at <http://steck.us/alkalidata>. We hope that this summary will serve experimental and theoretical researchers working with ytterbium, whether for atomic physics, quantum simulation, or metrology. Comments, corrections, and suggestions for improving this document are welcomed and encouraged.

* r.kroeze@lmu.de

† skristensen@atom-computing.com; Present address: Atom Computing, Inc., 2500 55th St, Boulder, Colorado 80301, USA

‡ sebastian.pucher@protonmail.com

2. STATISTICAL METHODS

This Section outlines the statistical methods used to combine and report the numerical values derived from multiple experimental or theoretical sources. If more than one value is cited for quantities such as the transition frequency, the lifetime of a state, the isotope shift, or the scattering length, the quoted value is a weighted mean of the values from the references, calculated as

$$\mu = \frac{\sum_{j=1}^n x_j / \sigma_j^2}{\sum_{j=1}^n 1 / \sigma_j^2}, \quad (1)$$

where x_j are the measurement values with uncertainties σ_j , and ($j = 1, \dots, n$) indexes the individual references. Here, the weights are the inverse squares of the uncertainties. The corresponding standard uncertainty in the weighted mean is

$$\sigma_\mu = \sqrt{\frac{1}{\sum_{j=1}^n 1 / \sigma_j^2}}. \quad (2)$$

If the measurements are not statistically consistent (i.e., the scatter exceeds what is expected from the reported uncertainties), we scale the uncertainty in the mean by the Birge ratio [10], defined as

$$R_B = \sqrt{\frac{1}{n-1} \sum_{j=1}^n \frac{(x_j - \mu)^2}{\sigma_j^2}} = \sqrt{\frac{\chi^2}{n-1}}, \quad (3)$$

where χ^2 is the chi-squared value and n is the number of data points. The final uncertainty in the mean is then

$$\sigma_\mu^{\text{adj}} = R_B \cdot \sigma_\mu. \quad (4)$$

If $R_B > 1$ for one dataset, we show R_B next to the reported weighted mean to indicate that the measured values are statistically inconsistent, and that we adjusted the uncertainty with the Birge ratio. We note that alternative techniques for assessing the uncertainty of a weighted mean are actively being investigated and may be employed in future updates [11].

When an experimental reference reports both a statistical uncertainty σ_{stat} and a systematic uncertainty σ_{sys} for a single measurement, the uncertainties are assumed to be uncorrelated. Hence, we combine the two contributions in quadrature to give the total one-sigma uncertainty

$$\sigma = \sqrt{\sigma_{\text{stat}}^2 + \sigma_{\text{sys}}^2}. \quad (5)$$

In cases where only asymmetric limits are provided, e.g., $x_0^{+\Delta x_+}_{-\Delta x_-}$, we obtain a single symmetric uncertainty by taking the larger deviation

$$\sigma = \max(\Delta x_+, \Delta x_-). \quad (6)$$

Reporting $x_0(\sigma) = x_0 \pm \sigma$ then guarantees coverage of both published bounds. Although this approach overestimates the error when the true distribution is asymmetric, it provides a straightforward, conservative uncertainty for tables and figures.

If an individual experimental reference reports multiple results for the same observable, and does not further combine these into a single value, we first perform this step ourselves using the framework described above, prior to comparing this average with other references. We note that if all results are mutually consistent, the order of this operation is irrelevant and the same μ and σ_μ would be obtained if all results would be averaged together once. If there are inconsistencies, this can lead to subtle differences in σ_μ .

3. YTTERBIUM PROPERTIES

Ytterbium (Yb) is a soft, malleable, and ductile rare-earth metal with a bright silvery luster. Although it oxidizes slowly in air, it should be stored in sealed containers to prevent degradation from moisture and oxygen. The metal reacts slowly with water but is readily attacked by both dilute and concentrated mineral acids [12]. Due to its reactivity, contaminated tools and surfaces can be cleaned with care using water or dilute acid solutions. In

powdered form (i.e., small grains or dust), ytterbium is significantly more reactive due to its increased surface area. Ytterbium has 70 electrons, two of which occupy the outermost shell. Natural ytterbium consists of seven stable isotopes, alongside more than 32 known unstable isotopes [13, 14]. This review focuses on the stable isotope ^{171}Yb .

Table 1 lists selected fundamental physical constants from the 2022 CODATA recommended values [15] that we use in this reference. In Table 2, key physical properties of the isotope ^{171}Yb are summarized. This isotope has a nuclear spin of $1/2$, resulting in fermionic particle statistics. The mass is the recommended value from the 2020 Atomic Mass Evaluation (AME2020) [16], and the relative natural abundance is from the characterization in Ref. [17] which was used to update the IUPAC standard atomic weight of Yb [18]. Abundance, mass, and nuclear spin of all stable Yb isotopes is provided in Table 3.

Thermodynamic properties such as density, molar volume, melting and boiling points as well as heat capacity are taken from Refs. [12, 19], and are given for naturally occurring Yb rather than the specific isotope ^{171}Yb . The vapor pressure at a temperature of $T = 25^\circ\text{C}$, as well as the temperature-dependent vapor pressure curve shown in Fig. 1, are calculated using the semi-empirical equation describing solid Yb provided in Ref. [20]:

$$\log_{10}(P) = 9.111 + \log_{10}(101\,325) - \frac{8111}{T} - 1.0849 \log_{10}(T), \quad (7)$$

where P is the vapor pressure in pascals, and T is the temperature in Kelvin. This expression is valid from $T = 298\text{ K}$ to $T = 900\text{ K}$. Over this range, it reproduces the experimental vapor pressure with an accuracy better than $\pm 5\%$. The first ionization energy (also called the ionization potential) of Yb has been measured through a variety of experimental techniques [21–29]. All but one of these measurements have insufficient precision to resolve isotope effects: based on mass-scaling one expects a relative difference in ionization energy of, e.g., $m_e/m(^{171}\text{Yb}) - m_e/m(^{174}\text{Yb}) \approx 5.5 \times 10^{-8}$ [30]. The only high-precision measurement in Ref. [22], performed for ^{174}Yb , has an uncertainty of about one order of magnitude smaller than this expected isotope effect. We thus take the isotope dependence into account by converting to ^{171}Yb prior to combining with the other measurements, resulting in the center-of-gravity ionization energy E_I in ^{171}Yb as listed in Table 2. Due to hyperfine interaction, two separate ionization energies can be found, as we further discuss in Section 4.1.

Low-energy elastic collisions between atoms are characterized by the s -wave scattering length a and play a central role in ultracold gas experiments [31]. For example, the magnitude of the scattering length governs the rate of thermalization during evaporative cooling, and the sign of a determines stability and collective phenomena of degenerate gases [32]. In alkali atoms, a can be magnetically tuned via Feshbach resonances to nearly arbitrary values $(-\infty, +\infty)$ [32]. In contrast, alkaline-earth atoms such as Yb have a ground state with zero electronic angular momentum, making them largely insensitive to magnetic tuning. For these systems, the ground-state scattering length is given by the binding energy of the highest vibrational state of the ground-state molecular potential. (We note that Feshbach resonances, however, have been shown to exist in a cold-atom ensemble of mixtures of electronic states, as described below.) Thanks to this simple dependence, experimentally accessible scattering lengths can be extrapolated to other isotope combinations using the Born-Oppenheimer approximation and a mass-scaling argument [33, 34]. Thus far, measurements have been limited to collisions between identical isotopes, as in Refs. [35–40], which are summarized on the diagonal of Table 4. For collisions between different isotopes, corresponding to the off-diagonal elements of Table 4, the results follow from mass-scaling as described in Refs. [35, 36]. This inter-isotope scattering is frequently used in cooling to degeneracy of ^{171}Yb , which can be achieved via sympathetic evaporative cooling with ^{174}Yb or ^{173}Yb [41–43]. (Other isotopes have likewise been sympathetically cooled [44].) Both ^{174}Yb and ^{173}Yb themselves can be evaporatively cooled to degeneracy, the former straightforwardly [39], the latter thanks to its large nuclear-spin subspace enabling collisions [38].

In addition to the electronic ground state, the metastable $^3\text{P}_0$ and $^3\text{P}_2$ states are sufficiently long-lived that it is meaningful to consider their scattering properties. Elastic s -wave scattering has been quantified in, e.g., Refs. [45–47]. Interorbital scattering, that is, scattering between one atom in $^1\text{S}_0$ and another in $^3\text{P}_{0,2}$, hosts rich physics and Feshbach resonances [45–54] and goes beyond the scope of this document. Finally, we note that *inelastic* scattering involving one or multiple atoms in the metastable states can induce significant loss, especially at high density. Again, recent work has quantified some of these loss rates [45–47, 49, 51, 52, 55–58] and we refrain from a detailed treatment.

4. LEVEL STRUCTURE

Ytterbium’s level structure is governed by its electronic configuration, which in its ground state is $[\text{Xe}]4f^{14}6s^2$. Its closed f-shell and two valence electrons in the 6s orbital result in an electronic structure that closely resembles that of alkaline-earth atoms. For this reason, Yb is often referred to as an *alkaline-earth-like* element. In analogy to helium and alkaline-earth atoms such as Sr and Mg, the two-electron configuration gives rise to singlet and triplet manifolds, well described in the Russell-Saunders (L-S) coupling scheme [59]. Figure 2 shows the energy levels and

transitions discussed in this reference, while Fig. 3 displays all Yb levels that can be found in the NIST Atomic Spectra Database [60]. Levels without an assigned LS-coupling term are grouped in the rightmost column, labeled ‘Other’. This includes, for example, states involving inner-shell excitations or states identified only by j–j coupling. The electronic level structure features both broad electric-dipole-allowed transitions with linewidths on the order of megahertz and narrow intercombination lines between singlet and triplet manifolds, with natural linewidths spanning millihertz to kilohertz.

Atomic-level notation generally consists of two parts: the electronic configuration and the term symbol. For the configuration, a sequence such as $n_1 l_1 n_2 l_2 \dots$ indicates which orbitals are occupied by the electrons. For example, 6s6p means that one electron is in the 6s orbital and one in the 6p orbital. In the term symbol $^{2S+1}L_J$, the superscript $2S + 1$ is the spin multiplicity, where S is the total (electronic) spin quantum number ($2S + 1 = 1$ for singlet, $2S + 1 = 3$ for triplet). The letter L encodes the total (electronic) orbital angular momentum (S for $L = 0$, P for $L = 1$, D for $L = 2$, etc.). The subscript J is the total (electronic) angular momentum. The resulting label

$$n_1 l_1 n_2 l_2 \dots {}^{2S+1}L_J \quad (8)$$

specifies both which orbitals the electrons occupy as well as the combined spin and orbital angular momentum quantum numbers of the entire atom (except its nucleus). In practice, and as already was done in Section 1, when the electrons unambiguously occupy the lowest-possible energy configuration for a given term symbol, these get omitted from the notation. As such, the electronic ground state $[\text{Xe}]4f^{14}6s^2 {}^1\text{S}_0$ will be shortened to ${}^1\text{S}_0$ and, e.g., ${}^3\text{D}_1$ denotes $[\text{Xe}]4f^{14}5d6s {}^3\text{D}_1$.

4.1. Energy Level Splittings

In Yb, each electronic term is split by spin-orbit (fine-structure) interactions into levels of different total electronic angular momentum \mathbf{J} , which arises from coupling the orbital (\mathbf{L}) and spin (\mathbf{S}) angular momenta of the electrons:

$$\mathbf{J} = \mathbf{L} + \mathbf{S} . \quad (9)$$

The magnitude of \mathbf{J} is given by $\hbar\sqrt{J(J+1)}$, where the integer quantum number J lies in the range

$$|L - S| \leq J \leq L + S . \quad (10)$$

The ground state ${}^1\text{S}_0$ has $L = 0$ and $S = 0$, yielding $J = 0$ and thus no fine-structure splitting. The lowest electronic excited states, where one of the electrons is promoted from 6s to 6p, has $L = 1$ and $S = 1$ so that $J = 0, 1, 2$ resulting in the fine-structure levels ${}^3\text{P}_0$, ${}^3\text{P}_1$, and ${}^3\text{P}_2$.

Beyond the electronic configuration, the nucleus can also contribute angular momentum. The fermionic isotope ${}^{171}\text{Yb}$ has a nuclear spin $I = 1/2$, which couples with the electronic angular momentum to form the total atomic angular momentum

$$\mathbf{F} = \mathbf{J} + \mathbf{I} , \quad (11)$$

where the quantum number F is restricted to

$$|J - I| \leq F \leq J + I , \quad (12)$$

and again F sets the magnitude of \mathbf{F} via $\hbar\sqrt{F(F+1)}$. States with $J = 0$ have $F = I = 1/2$. Hence, states such as ${}^1\text{S}_0$ and ${}^3\text{P}_0$ exhibit no hyperfine splitting and therefore form an ideal nuclear-spin qubit [61–63]. States with $J > 0$, however, are separated into hyperfine multiplets. To understand the shift of these levels, only the magnetic dipole interaction has to be considered, since $I = 1/2$ causes higher order hyperfine interactions such as the electric quadrupole to vanish. In that case, the hyperfine Hamiltonian is given by

$$H_{\text{hfs}} = A_{\text{hfs}} \mathbf{I} \cdot \mathbf{J} , \quad (13)$$

where A_{hfs} is the magnetic dipole constant (which itself depends on L , S and J). The resulting energy shift for a hyperfine level is given by [64]

$$\Delta E_{\text{hfs}} = \frac{1}{2} A_{\text{hfs}} K , \quad (14)$$

where

$$K = F(F+1) - J(J+1) - I(I+1) . \quad (15)$$

It can be straightforwardly verified that the average of all hyperfine shifts, weighted by the number of sublevels $2F + 1$ in each manifold, is zero (even when higher-order hyperfine interactions are included).

As stated, the magnetic dipole constant A_{hfs} varies between electronic levels of ^{171}Yb , and can be measured through spectroscopic investigations. The results are summarized in Table 5. For $^1\text{P}_1$, no less than 11 papers have reported original values for the hyperfine coefficient. These are combined according to Section 2, but are dominated by the result from Ref. [65]. We note that the accuracy of that measurement was subsequently questioned, see for example the discussion in Ref. [66]. If Ref. [65] is excluded the remaining results nonetheless remain inconsistent, yielding $A_{\text{hfs}}(^1\text{P}_1)/h = -212.2(4)$ MHz (R_B : 1.8). The literature also yields inconsistent results for many of the other levels, though not with a clear single outlier. Finally, we note that we were not able to verify Refs. [67, 68] in any original source material and instead rely on the values reported in Ref. [66] and Ref. [69], respectively.

The presence of hyperfine coupling leads to an ionization structure in ^{171}Yb that is qualitatively different from that of ^{174}Yb , which has $I = 0$. In ^{171}Yb , the Rydberg states exhibit strong hyperfine interactions, originating from the interplay between the hyperfine coupling in the ionic Yb^+ core and the exchange interaction with the Rydberg electron [63]. This situation is nearly the opposite of alkali-metal atoms: in alkali-metal atoms, the neutral ground state has strong hyperfine coupling while the Rydberg states are largely unaffected, whereas in ^{171}Yb the ground state has no hyperfine interaction and the Rydberg states split strongly [63, 70]. As a result, the Rydberg series of ^{171}Yb converge to two distinct ionization thresholds E_I^0 and E_I^1 [63]. These thresholds can be associated with the hyperfine-splitting of the $^{171}\text{Yb}^+$ ground state $6s^2\text{S}_{1/2}$, which splits into $F_{\text{core}} = 0$ and $F_{\text{core}} = 1$ states separated by the ionic hyperfine constant $A_{\text{hfs}}(6s^2\text{S}_{1/2})$ [71]. By combining high-resolution spectroscopy with multichannel quantum defect theory, Ref. [63] determined both thresholds, the values of which are listed in Table 2.

4.2. Interaction with Magnetic Fields

External magnetic fields will further affect the energy levels beyond the fine-structure and hyperfine-structure interactions considered above. The Hamiltonian describing the interaction of atomic electrons and nuclear spins with a static magnetic field \mathbf{B} , which defines a quantization axis taken here to be the z -axis, is given by

$$H_B = \frac{\mu_B}{\hbar} (g_S \mathbf{S} + g_L \mathbf{L} + g_I \mathbf{I}) \cdot \mathbf{B} = \frac{\mu_B}{\hbar} (g_S S_z + g_L L_z + g_I I_z) B_z, \quad (16)$$

where μ_B is the Bohr magneton, g_S , g_L , and g_I are the electron spin, orbital and nuclear g -factors respectively, and S_z , L_z , and I_z denote angular momentum components along the z -axis. We note explicitly that the nuclear term here is written with the prefactor μ_B ; in an alternative convention, commonly found in nuclear physics, the prefactor is μ_N , resulting in a value of g_I larger by a factor μ_B/μ_N , where μ_N is the nuclear magneton.

The value for g_S has been measured precisely, and we list the CODATA recommended value in Table 2. The orbital g -factor is corrected for finite nuclear mass by [72]

$$g_L = 1 - \frac{m_e}{m_{\text{nuc}}}, \quad (17)$$

where m_e is the electron mass and m_{nuc} is the nuclear mass, accurate to leading order in m_e/m_{nuc} . The nuclear g -factor g_I is experimentally determined from measurements of the nuclear magnetic moment μ . Given the nuclear spin I , g_I can be calculated using¹

$$g_I = -\frac{\mu}{\mu_B I}. \quad (18)$$

For ^{171}Yb , μ has been measured in Refs. [74–76] and subsequently tabulated in, e.g., Refs. [77–79]. We report the value stated in the most recent tabulation of Ref. [73], which corrects the earlier results for updates to fundamental constants, various nuclear magnetic effects, and aims to establish a ‘best’ value, see the discussion therein. It states

$$\mu = 0.4923(4)\mu_N, \quad (19)$$

so that $g_I = -0.000\,536\,2(4)$.

In general, calculating the energy levels involves diagonalizing the combined hyperfine and magnetic Hamiltonians, $H_{\text{hfs}} + H_B$. The resulting energy shifts of the hyperfine structure in an external magnetic field are shown in Fig. 8.

¹ The minus sign here is due to our sign convention in the magnetic Hamiltonian, where we have the term $+g_I \mathbf{I} \cdot \mathbf{B}$, and is consistent with Refs. [1–4] versus Ref. [73] where μ and g_I have opposite sign.

We calculate shifts for all hyperfine (F) levels within a given fine-structure state, neglecting any coupling to other fine-structure states. As a result, the calculations are valid only in the regime where the Zeeman interaction is small compared to the fine-structure splitting. At higher magnetic fields, particularly for the $^3\text{P}_0$ clock state, fine-structure mixing becomes non-negligible, and a more comprehensive treatment is required to accurately capture the Zeeman effect (see, e.g., Ref. [80]). We now turn to a discussion of low- and high-magnetic-field regimes where approximations can be found.

4.2.1. Weak Field Limit – Zeeman Effect

In the limit of weak magnetic fields, where energy shifts are small compared to hyperfine splittings, F is a good quantum number. The magnetic Hamiltonian can then be written as

$$H_B = \frac{\mu_B}{\hbar} g_F F_z B_z, \quad (20)$$

where the hyperfine Landé factor g_F is given by

$$g_F = g_J \frac{F(F+1) - I(I+1) + J(J+1)}{2F(F+1)} + g_I \frac{F(F+1) + I(I+1) - J(J+1)}{2F(F+1)}, \quad (21)$$

and the electronic Landé factor is

$$g_J = g_L \frac{J(J+1) - S(S+1) + L(L+1)}{2J(J+1)} + g_S \frac{J(J+1) + S(S+1) - L(L+1)}{2J(J+1)}. \quad (22)$$

The operator F_z acts as

$$F_z |F, m_F\rangle = \hbar m_F |F, m_F\rangle, \quad (23)$$

where m_F is the magnetic quantum number for the projection of \mathbf{F} on the quantization axis ($|m_F| \leq F$ so that there are $2F + 1$ different m_F -levels). The degeneracy of each hyperfine manifold is thus lifted via the first-order Zeeman shift,

$$\Delta E_{F, m_F} = \hbar \Delta \omega_{F, m_F} = \mu_B g_F m_F B_z. \quad (24)$$

For states with $J \neq 0$, the value of g_F is dominated by g_J . We note however, that the above framework arises from an effectively first-order perturbation theory treatment. Further corrections to g_J arise from the multi-electron structure, and additional contributions stem from, e.g., QED effects [72, 81, 82]. As such, in Table 5 we summarize the g_J coefficient as well as the Zeeman coefficient for each level considered in this document. Where possible, these follow from an experimental characterization of g_J , with indicated references. If no such data exists, we revert back to the above expressions, and shall indicate this with an asterisk. For the optical clock states $^1\text{S}_0$ and $^3\text{P}_0$, there is no g_J and Eq. (21) yields $g_F = g_I$ for both states. However, these states have an easily resolvable differential Zeeman shift [49, 50, 83, 84]. This arises due to the hyperfine interaction that induces state mixing (see also Section 4.3) [80], and yields a nuclear Landé factor for $^3\text{P}_0$ that is given by $g_I(^3\text{P}_0) = g_I(^1\text{S}_0) + g_{\text{hfs}}$. Combining the results from the above references, we find $g_{\text{hfs}} = -0.000\,142\,549\,6(14)$; the reported Zeeman coefficient in Table 5 takes this effect into account. For $^3\text{D}_1$, measured Zeeman shifts are reported in Refs. [85, 86], however we note that the measurements therein are far away from the theoretical values without any given explanation. For this level, we thus choose to report the theoretical values in Table 5.

Of further importance to the $^1\text{S}_0$ and $^3\text{P}_0$ states is the higher-order, quadratic Zeeman shift, arising due to the fine-structure interaction inducing state mixing (see again Section 4.3) [80]. The total magnetic field shift to the clock transition is thus given by

$$\Delta \omega_B(\mathbf{B}) = \mu_B g_I (m_{F'} - m_F) B + \mu_B g_{\text{hfs}} m_{F'} B + \eta B^2, \quad (25)$$

where B is the magnitude of the magnetic field, and η is the quadratic Zeeman shift coefficient. Optical lattice clocks have characterized this effect in detail. Since a negligible difference is expected between isotopes [80], we include measurements from across all isotopes [49, 83, 84, 87–93]. This results in $\eta = -0.060\,84(6) \text{ Hz/G}^2$ (R_B : 1.2). The value reported in Ref. [84], which most strongly influences this average, has recently been corrected in Ref. [94]. With it, the average changes to $\eta = -0.060\,21(12) \text{ Hz/G}^2$ (R_B : 2.1). Similar corrections arising from updates to, e.g., nuclear magnetic moments and diamagnetic correction factors might apply to the other references as well, however this is beyond the scope of this document.

4.2.2. Strong Field Limit – Paschen-Back Regime

For strong magnetic fields, the strength of H_B can exceed the hyperfine interaction. In this Paschen-Back regime, F is no longer the appropriate quantum number with which to index the sublevels. (We note that this regime does not exist for 1S_0 and 3P_0 as they lack hyperfine structure, or in other words $L = S = 0$ so that $F = I$ is always a good quantum number.) Provided the magnetic interaction is not so strong that it also overwhelms the fine-structure coupling, J and I along with their projections m_J and m_I determine the eigenstates of the atom. This results in energy shifts given by

$$\Delta E_{\text{Paschen-Back}} = A_{\text{hfs}} m_I m_J + \mu_B (g_J m_J + g_I m_I) B. \quad (26)$$

The relevant quantities for this expression have been discussed above and can be found in Table 5.

4.3. State Mixing

In fermionic ^{171}Yb , state mixing in the $6s6p$ manifold arises from three key mechanisms: spin-orbit coupling, hyperfine coupling, and Zeeman interactions. Each contributes to the admixture of nominally pure states $^{2S+1}L_J^{(0)}$ leading to the physical states $^{2S+1}L_J$. This mixing enables otherwise forbidden transitions. Here, we describe the state mixing following the methods in Refs. [89, 95, 96].

4.3.1. Spin-Orbit Coupling

Spin-orbit coupling is the fundamental source of singlet-triplet mixing in Yb, present even in the absence of nuclear spin or external fields. In the $6s6p$ manifold, the $J = 1$ subspace splits into 3P_1 and 1P_1 states, which are related to the pure spin-orbit basis by the unitary transform

$$\begin{pmatrix} |^1P_1^{(\text{so})}\rangle \\ |^3P_0^{(\text{so})}\rangle \\ |^3P_1^{(\text{so})}\rangle \\ |^3P_2^{(\text{so})}\rangle \end{pmatrix} = \begin{pmatrix} \alpha & 0 & -\beta & 0 \\ 0 & 1 & 0 & 0 \\ \beta & 0 & \alpha & 0 \\ 0 & 0 & 0 & 1 \end{pmatrix} \begin{pmatrix} |^1P_1^{(0)}\rangle \\ |^3P_0^{(0)}\rangle \\ |^3P_1^{(0)}\rangle \\ |^3P_2^{(0)}\rangle \end{pmatrix}, \quad (27)$$

with $\alpha^2 + \beta^2 = 1$. The singlet-triplet mixing in the $J = 1$ manifold can be extracted directly from measured lifetimes and transition frequencies by assuming that the bare $^3P_1^{(0)}$ state has zero E1 decay rate and that the entire observed decay rate of 3P_1 arises from spin-orbit coupling with the $^1P_1^{(0)}$ state. One can then find the relation [80, 96]

$$\frac{\beta^2}{\alpha^2} = \frac{\Gamma_{3P_1} \nu^3(^1S_0 - ^1P_1)}{\Gamma_{1P_1} \nu^3(^1S_0 - ^3P_1)}, \quad (28)$$

where Γ_i are the decay rates of the states and ν_i the transition frequencies between the ground and the excited states. Using the values of Tables 8 and 10, we find

$$\beta = -0.12905(19), \quad \text{and} \quad \alpha = \sqrt{1 - \beta^2} = 0.991638(25),$$

corresponding to a singlet admixture of approximately 1.7% in the 3P_1 state. Note that the NIST database for Yb lists leading percentages for various states, which indicate the dominant configuration components of each eigenstate and thus quantify the degree of state mixing [60]. The negative sign of β can be inferred from the derivation of the intermediate coupling coefficients in [95]. As a result, the otherwise forbidden intercombination line acquires a finite electric-dipole matrix element

$$\langle ^1S_0 | \hat{\mathbf{d}} | ^3P_1^{(\text{so})} \rangle = \beta \langle ^1S_0 | \hat{\mathbf{d}} | ^1P_1^{(0)} \rangle \neq 0. \quad (29)$$

4.3.2. Hyperfine Coupling

The nonzero nuclear spin $I = 1/2$ of ^{171}Yb gives rise to the hyperfine Hamiltonian in Eq. (13). This leads to a hyperfine coupling between states with different J but the same total F and m_F . For example, to first order, the clock state is given by

$$|{}^3\text{P}_0\rangle = |{}^3\text{P}_0^{(\text{so})}\rangle + \alpha_0 |{}^3\text{P}_1^{(\text{so})}\rangle + \beta_0 |{}^1\text{P}_1^{(\text{so})}\rangle . \quad (30)$$

Together with Eq. (27), we can relate the physical states to the pure states

$$\begin{pmatrix} |{}^1\text{P}_1, F = \frac{1}{2}\rangle \\ |{}^1\text{P}_1, F = \frac{3}{2}\rangle \\ |{}^3\text{P}_0, F = \frac{1}{2}\rangle \\ |{}^3\text{P}_1, F = \frac{1}{2}\rangle \\ |{}^3\text{P}_1, F = \frac{3}{2}\rangle \\ |{}^3\text{P}_2, F = \frac{3}{2}\rangle \\ |{}^3\text{P}_2, F = \frac{5}{2}\rangle \end{pmatrix} = \begin{pmatrix} \alpha & 0 & -\beta_0 & -\beta & 0 & 0 & 0 \\ 0 & \alpha & 0 & 0 & -\beta & -\beta_2 & 0 \\ \beta_0\alpha + \alpha_0\beta & 0 & 1 & -\beta_0\beta + \alpha_0\alpha & 0 & 0 & 0 \\ \beta & 0 & -\alpha_0 & \alpha & 0 & 0 & 0 \\ 0 & \beta & 0 & 0 & \alpha & -\alpha_2 & 0 \\ 0 & \beta_2\alpha + \alpha_2\beta & 0 & 0 & -\beta_2\beta + \alpha_2\alpha & 1 & 0 \\ 0 & 0 & 0 & 0 & 0 & 0 & 1 \end{pmatrix} \begin{pmatrix} |{}^1\text{P}_1^{(0)}, F = \frac{1}{2}\rangle \\ |{}^1\text{P}_1^{(0)}, F = \frac{3}{2}\rangle \\ |{}^3\text{P}_0^{(0)}, F = \frac{1}{2}\rangle \\ |{}^3\text{P}_1^{(0)}, F = \frac{1}{2}\rangle \\ |{}^3\text{P}_1^{(0)}, F = \frac{3}{2}\rangle \\ |{}^3\text{P}_2^{(0)}, F = \frac{3}{2}\rangle \\ |{}^3\text{P}_2^{(0)}, F = \frac{5}{2}\rangle \end{pmatrix} . \quad (31)$$

Here, the hyperfine coupling constants can be inferred from experimentally measured hyperfine splittings in the singlet and triplet manifold using the Breit-Wills theory, see e.g., Ref. [80]. The dominant dipole-mediated term α_0 is almost two orders of magnitude larger than the singlet term β_0 [89], and it produces an intrinsic electric-dipole matrix element for the clock transition which corresponds to a zero-field linewidth of ~ 8 mHz. This hyperfine-induced E1 coupling is therefore sufficient for direct clock spectroscopy without any external mixing magnetic field, unlike in bosonic isotopes.

4.3.3. Zeeman Coupling

An external magnetic field \mathbf{B} couples states via the Hamiltonian H_B in Eq. (16). In the mixed basis, H_B produces both Zeeman shifts and further state admixture. A static magnetic field B can be applied to mix the $|{}^3\text{P}_0\rangle$ state with the $|{}^3\text{P}_1\rangle$ state via the magnetic-dipole operator $\hat{\mu}$ [97]

$$|{}^3\text{P}'_0\rangle = |{}^3\text{P}_0\rangle + \frac{\langle{}^3\text{P}_1|\hat{\mu}\cdot B|{}^3\text{P}_0\rangle}{\Delta_{10}} |{}^3\text{P}_1\rangle , \quad (32)$$

where $\Delta_{10} \equiv \omega_{3\text{P}_1} - \omega_{3\text{P}_0} \approx 2\pi \times 21.1$ THz, see values in Tables 9 and 10. Since $|{}^3\text{P}_1\rangle$ itself carries the small β -admixture of $|{}^1\text{P}_1^{(0)}\rangle$, the doubly-mixed clock state becomes

$$|{}^3\text{P}'_0\rangle = |{}^3\text{P}_0\rangle + \frac{\langle{}^3\text{P}_1|\hat{\mu}\cdot B|{}^3\text{P}_0\rangle}{\Delta_{10}} (\alpha |{}^3\text{P}_1^{(0)}\rangle + \beta |{}^1\text{P}_1^{(0)}\rangle - \alpha_0 |{}^3\text{P}_0^{(0)}\rangle) . \quad (33)$$

This second-order effect produces the quadratic Zeeman shift of the clock frequency, and a residual field-dependent linewidth

$$\Gamma_{\text{clock}}(B) = \Gamma_{3\text{P}_0} + \Gamma_{3\text{P}_1} \frac{(\mu_C B)^2}{2\Delta_{10}^2} , \quad \mu_C = \sqrt{\frac{2}{3}} (g_L - g_S) \mu_B , \quad (34)$$

where the zero-field decay rate $\Gamma_{3\text{P}_0} \approx 2\pi \times 8$ mHz arises from hyperfine-induced mixing, and the field-dependent term remains at the mHz level even for $B \sim 1$ kG.

5. TRANSITION PROPERTIES

This Section examines the key atomic transitions. Measured transition frequencies are presented and converted to wavelengths and transition energies. Experimentally determined lifetimes of the excited states are reviewed. Equations for obtaining additional parameters from these transition frequencies and lifetimes are introduced.

We note that we only consider direct measurements of the quantity of interest, with the caveat that this approach can lead to inconsistencies when combining different results. For example, the energy difference between 3S_1 and 1S_0 can be obtained by using the absolute transition frequency measurements on the pathways $^1S_0 \rightarrow ^3P_0 \rightarrow ^3S_1$ versus $^1S_0 \rightarrow ^3P_2 \rightarrow ^3S_1$, yielding a difference of $2\pi \times -0.15(4)$ GHz. Alternatively, some experiments, such as in Ref. [98], directly measure energy-separation of two states without absolute accuracy of either transition, though these then are omitted from inclusion in any of the Tables. A few exceptions to this general approach are noted below.

5.1. Transition Frequencies and Wavelengths

The following relations allow one to convert a transition frequency $\omega_0 = 2\pi \times \nu$ to the corresponding transition energy, vacuum wavelength, air wavelength, and wavenumber. The photon energy E is

$$E = h\nu = \hbar\omega_0 . \quad (35)$$

This transition energy can be converted into an energy in eV using

$$E_{\text{eV}} = \frac{h\nu}{e} = \frac{\hbar\omega_0}{e} . \quad (36)$$

The vacuum wavelength λ and the angular wavenumber k_L are

$$\lambda = \frac{c}{\nu} = \frac{2\pi c}{\omega_0} , \quad (37)$$

$$k_L = \frac{2\pi}{\lambda} = \frac{\omega_0}{c} . \quad (38)$$

The wavelength in air is given by

$$\lambda_{\text{air}} = \frac{\lambda}{n_{\text{air}}} , \quad (39)$$

where n_{air} is the refractive index of air. To compute the refractive index of air under typical laboratory conditions, the Edlén's equation is a common approximation [99, 100]

$$n_{\text{air}} = 1 + \left[\left(8342.54 + \frac{2406147}{130 - \kappa^2} + \frac{15998}{38.9 - \kappa^2} \right) \frac{P}{96095.43} \frac{1 + 10^{-8}(0.601 - 0.00972 T)P}{1 + 0.0036610 T} - f(0.037345 - 0.000401\kappa^2) \right] \times 10^{-8} , \quad (40)$$

where $\kappa = k_L/(2\pi)$ is the vacuum wavenumber in $1/\mu\text{m}$, P is the total air pressure in Pa, T is the temperature in $^\circ\text{C}$, and f is the partial pressure of water vapor in Pa (obtainable from relative humidity via the Buck equation [101, 102]). Under standard conditions ($P = 101325$ Pa, $T = 25$ $^\circ\text{C}$, 50% relative humidity), this yields $n_{\text{air}} \approx 1.00027$ in the visible range with a 1σ uncertainty of 1×10^{-8} which has been used throughout this reference. In real-world applications, additional uncertainties due to fluctuations in pressure, temperature, and humidity must be considered and are not included here, see for example Refs. [1–4].

In precision spectroscopy one often measures transition frequencies $\nu_{F_g \rightarrow F_e}$ between specific hyperfine levels F_g and F_e of the ground and excited state, respectively. Each of these measured transitions is (potentially) shifted due to the hyperfine shift, Eq. (14). We instead report the absolute transition frequencies between the ‘bare’ levels, corresponding to the center-of-gravity or centroid of the hyperfine levels. As described after Eq. (14), this center-of-gravity energy level can be determined by a weighted sum over the hyperfine manifolds. Likewise, the center-of-gravity transition frequency can be determined via a weighted sum of the individual transition frequencies $\nu_{F_g \rightarrow F_e}$. However, to correctly perform this weighted average, the weights $W_{F_g \rightarrow F_e}$ additionally need to take into account the selection rules that forbid certain transitions. The correct weights to achieve this are given by [103]

$$W_{F_g \rightarrow F_e} = (2F_g + 1)(2F_e + 1) \left\{ \begin{matrix} J_e & F_e & I \\ F_g & J_g & 1 \end{matrix} \right\}^2 , \quad (41)$$

where the term in the curly brackets is the Wigner 6- j symbol and depends also on the total electronic angular momentum $J_{g,e}$ of both states. The transition frequency is then given by

$$\nu_{\text{cg}} = \sum_{F_g, F_e} W_{F_g \rightarrow F_e} \nu_{F_g \rightarrow F_e} \bigg/ \sum_{F_g, F_e} W_{F_g \rightarrow F_e} . \quad (42)$$

If a reference does not explicitly state ν_{cg} but reports all required transition frequencies $\nu_{F_g \rightarrow F_e}$, we consider all corresponding uncertainties as independent and evaluate ν_{cg} using the above expression. The propagated uncertainty of the center-of-gravity frequency is then given by

$$\sigma_{\text{cg}} = \sqrt{\sum_{F_g, F_e} W_{F_g \rightarrow F_e}^2 \sigma_{F_g \rightarrow F_e}^2} \bigg/ \sum_{F_g, F_e} W_{F_g \rightarrow F_e} . \quad (43)$$

The following comments apply for the absolute frequencies listed in Tables 8 to 14:

- For the $^1\text{S}_0 \rightarrow ^1\text{P}_1$ transition, Refs. [65, 66, 104–106] report absolute frequencies, giving an average of $2\pi \times 751.52706(12)$ THz (R_B : 1895). The extremely large R_B is primarily caused by Ref. [65], which has by far the smallest uncertainty but reports an absolute frequency different from the others by many times the natural linewidth of ~ 30 MHz, suggesting some systematic discrepancies. As discussed in the context of hyperfine splitting, the accuracy of the measurements reported in Ref. [65] has been questioned. For these reasons, in Table 8 we exclude Ref. [65] for figuring the absolute transition frequency.
- The $^1\text{S}_0 \rightarrow ^3\text{P}_0$ clock transition frequency has been subject of a large number of experimental studies [88, 91, 107–120]. Their combined absolute frequency is $518\,295\,836\,590\,863.62(5)$ Hz. However, in Table 9, we adopt the value from the 2021 CIPM recommendation published by the BIPM [121], which is endorsed by the CCTF as a secondary representation of the SI second [122].
- For the $^1\text{S}_0 \rightarrow ^3\text{P}_2$ transition, we use the value from Ref. [123], derived by combining the absolute frequency of the $^1\text{S}_0 \rightarrow ^3\text{P}_0$ transition from Ref. [120] with absolute frequency measurements of the $^3\text{P}_0 \rightarrow ^3\text{S}_1$ and $^3\text{P}_2 \rightarrow ^3\text{S}_1$ transitions.

Differences in nuclear mass and charge distribution result in changes of the transition frequencies across isotopes of Yb. These isotope shifts play important roles in beyond-Standard Model physics [124–126]. With its many stable isotopes, Yb is well-suited for such studies. Table 6 summarizes experimental measurements of these isotope shifts for the states considered here. All shifts are expressed relative to ^{174}Yb , as is customary in the literature. Note that we list the isotope shift of the *state* relative to the $^1\text{S}_0$ ground state, not the transition frequency. These are of course equivalent for transitions out of $^1\text{S}_0$, but for $^3\text{S}_1$ and $^3\text{D}_1$ we include measurements performed on transitions out of $^3\text{P}_{0,2}$. The latter are converted into state-shifts by adding the isotope shift of the corresponding lower state as listed elsewhere in the Table. To be abundantly clear, the listed quantities are $\Delta E_{\text{iso}}/h$, where

$$\Delta E_{\text{iso}} = [E(^{2S+1}L_J, ^A\text{Yb}) - E(^1\text{S}_0, ^A\text{Yb})] - [E(^{2S+1}L_J, ^{174}\text{Yb}) - E(^1\text{S}_0, ^{174}\text{Yb})] . \quad (44)$$

For the isotopes with hyperfine structure (i.e., ^{171}Yb and ^{173}Yb) we use the center-of-gravity E_{cg} as described following Eq. (14). The following comments apply:

- Across the $^3\text{P}_{0,1,2}$ states, the isotope shifts are expected to be nearly identical, and the same applies for $^3\text{D}_{1,2,3}$. Indeed the measured shifts for $^3\text{P}_0$ versus $^3\text{P}_1$ versus $^3\text{P}_2$ and $^3\text{D}_1$ versus $^3\text{D}_2$ reflect this.
- For $^3\text{S}_1$, when combining the pathways $^1\text{S}_0 \rightarrow ^3\text{P}_0 \rightarrow ^3\text{S}_1$ and $^1\text{S}_0 \rightarrow ^3\text{P}_2 \rightarrow ^3\text{S}_1$ as described above, we find significant Birge ratios. If only the former pathway is considered, the respective measurements are mutually consistent. We do not speculate on the exact cause of the inconsistencies.
- Again, the source material for Ref. [67] could not be consulted, so here we rely on the values reported in Refs. [127, 128].
- For the lowest-abundance isotope ^{168}Yb not all isotope shifts have been measured. Likewise, for the fermionic isotopes ^{171}Yb and ^{173}Yb , no isotope shifts for $^3\text{P}_2$ have been reported. Those cases where no measurement was found are indicated by a question mark.

5.2. Decay of Excited States

An excited state $|e\rangle$ that decays to several lower levels $\{|g_i\rangle\}$ is described by Einstein A -coefficients $A_{e\rightarrow g_i}$. The total spontaneous decay rate is

$$\Gamma = \sum_i A_{e\rightarrow g_i} . \quad (45)$$

The excited-state lifetime τ is directly related to the total spontaneous decay rate

$$\tau = \frac{1}{\Gamma} . \quad (46)$$

The corresponding full-width at half-maximum of the transition's line shape is

$$\Delta\nu_{\text{FWHM}} = \frac{\Gamma}{2\pi} . \quad (47)$$

Each decay channel i carries a branching ratio

$$\beta_i = \frac{A_{e\rightarrow g_i}}{\Gamma} , \quad (48)$$

so its partial decay rate is

$$\Gamma_{\text{partial}} = \beta_i \Gamma = A_{e\rightarrow g_i} . \quad (49)$$

Thus, combining a precise measurement of τ with known β_i directly yields the individual A -coefficients.

The following comments apply for the lifetimes and branching ratios listed in Tables 8 to 14:

- The metastable $^3\text{P}_2$ state can decay to the $^1\text{S}_0$ ground level via a magnetic-quadrupole (M2) transition. Additional decay arises from magnetic-dipole (M1) decay to $^3\text{P}_1$ and black-body-induced excitation to higher-lying triplet levels. In odd isotopes as ^{171}Yb , however, hyperfine mixing with the nearby $^3\text{P}_1$ and $^1\text{P}_1$ manifolds as described in Section 4.3 opens electric-dipole (E1) decay channels that dominate the radiative lifetime. For the $^3\text{P}_2$ state, to our knowledge no experimental measurement of its radiative lifetime has been performed. We therefore adopt a theoretical value in Table 11 [129]. Note that the lifetime in even isotopes is predicted to be significantly longer [129, 130].
- Likewise, we are unaware of any experimental results that completely characterize the branching ratios for any excited state. Ref. [131] contains a partial characterization of the branching out of $^1\text{P}_1$, finding a lower bound of $1.2(4) \times 10^{-7}$. This is in line with theoretical calculations [132], and most notably is two orders of magnitude smaller than the comparable atom Sr [5]. As such, the $^1\text{S}_0 \rightarrow ^1\text{P}_1$ transition can be effectively considered a cycling transition, allowing laser cooling without the need for additional repumping lasers. All stated branching ratios follow from theoretical calculations as detailed below.
- We were unable to find source material for Refs. [133–136]. Instead, we rely on values reported in Refs. [137–139].

5.3. Additional Transition Parameters

The spontaneous emission rate Γ determines the relative intensity of a spectral line. For a $J \rightarrow J'$ electric-dipole transition, Γ is directly linked to the absorption oscillator strength f via [140]

$$\Gamma = \frac{e^2 \omega_0^2}{2\pi \epsilon_0 m_e c^3} \frac{2J+1}{2J'+1} f . \quad (50)$$

The spontaneous decay rate for a two-level atom is related to the dipole matrix element d via [141]

$$\Gamma = \frac{\omega_0^3 |d|^2}{3\pi \epsilon_0 \hbar c^3} \implies |d|^2 = \frac{3\pi \epsilon_0 \hbar c^3}{\omega_0^3} \Gamma . \quad (51)$$

For a multi-level atom, the spontaneous decay rate between an excited state with total electronic angular momentum J_e and one of the lower levels with J_{g_i} is instead given by

$$\Gamma_{\text{partial}} = A_{e \rightarrow g_i} = \frac{\omega_{eg_i}^3}{3\pi\epsilon_0\hbar c^3} \frac{2J_{g_i} + 1}{2J_e + 1} |\langle J_{g_i} \| \mathbf{er} \| J_e \rangle|^2 = \frac{\omega_{eg_i}^3}{3\pi\epsilon_0\hbar c^3} \frac{1}{2J_e + 1} |\langle J_{g_i} \| \mathbf{er} \| J_e \rangle_R|^2 . \quad (52)$$

Here, $\langle J \| \mathbf{er} \| J' \rangle$ is the *reduced* dipole matrix element using the convention of, e.g., Refs. [142, 143], whereas the notation $\langle J \| \mathbf{er} \| J' \rangle_R = \sqrt{2J + 1} \langle J \| \mathbf{er} \| J' \rangle$ is reserved for the Racah-Wigner convention, used for example in Ref. [144]. These reduced dipole matrix elements relate to dipole matrix elements through invocation of the Wigner-Eckart theorem, described in detail in Section 6.3. The above expression can then be used together with Eq. (48) to calculate the branching ratios β_i between fine-structure states as

$$\beta_i = \frac{|\langle J_{g_i} \| \mathbf{er} \| J_e \rangle_R|^2 \omega_{eg_i}^3}{\sum_{g_i} |\langle J_{g_i} \| \mathbf{er} \| J_e \rangle_R|^2 \omega_{eg_i}^3} , \quad (53)$$

where the sum in the denominator runs over all allowed final states $\{|g_i\rangle\}$. We use this relation together with the values given in Ref. [132] to state the branching ratios in Tables 8 to 14. The reduced matrix elements are then found by reversing the above relation, to yield (up to a phase factor)

$$\langle J_{g_i} \| \mathbf{er} \| J_e \rangle_R = \sqrt{2J_e + 1} \sqrt{\frac{3\pi\epsilon_0\hbar c^3}{\omega_{eg_i}^3} \frac{\beta_i}{\tau_e}} , \quad (54)$$

which we evaluate using the experimental transition frequency ω_{eg_i} and excited state lifetime τ_e .

Absorbing or emitting a resonant photon of momentum $\hbar k_L$ changes the velocity of an atom by the recoil velocity

$$v_r = \frac{\hbar k_L}{m} . \quad (55)$$

The corresponding change in kinetic energy $\frac{1}{2}mv_r^2 = \frac{\hbar^2 k_L^2}{2m}$ can be written as a recoil energy $E_{\text{rec}} = \hbar\omega_r$, which defines the recoil frequency ω_r

$$E_{\text{rec}} = \hbar\omega_r = \frac{\hbar^2 k_L^2}{2m} \Rightarrow \omega_r = \frac{\hbar k_L^2}{2m} . \quad (56)$$

An atom moving at velocity $v \ll c$ sees the optical frequency ω_L shifted by a Doppler shift

$$\Delta\omega_d = \frac{v}{c} \omega_L . \quad (57)$$

In particular, for $v = v_r$ one finds $\Delta\omega_d = 2\omega_r$, showing that a single recoil kick corresponds to a twice as high Doppler shift change.

From these motions arise two key temperatures. The recoil temperature

$$T_r = \frac{\hbar^2 k_L^2}{m k_B} \quad (58)$$

is the temperature corresponding to an ensemble with a one-dimensional root-mean-square momentum of one photon recoil [4]. Note that the single-photon recoil energy E_{rec} (see Eq. (56)) can be expressed as a temperature via $k_B T = E_{\text{rec}}$, giving

$$T = \frac{\hbar^2 k_L^2}{2m k_B} , \quad (59)$$

which is exactly half of the rms-defined recoil temperature T_r . The Doppler temperature

$$T_D = \frac{\hbar \Gamma}{2 k_B} \quad (60)$$

is the lowest temperature that Doppler cooling of a two-level atom can reach, set by the balance of Doppler cooling and recoil heating [145]. Fermionic ^{171}Yb possesses Zeeman substructure in its $^1\text{S}_0$ ground state. This enables sub-Doppler cooling mechanisms (e.g., Sisyphus or polarization-gradient cooling) on the narrow $^1\text{S}_0 \rightarrow ^3\text{P}_1$ intercombination line.

5.4. Magneto-Optical Traps

Magneto-optical traps (MOTs) use laser light and magnetic fields to cool and confine neutral atoms. For the fermionic isotope ^{171}Yb , two transitions are typically used to cool the atoms in sequence to bring them from high thermal velocities to cold temperatures suitable for optical trapping or precision measurement.

The first cooling stage typically uses the strong $^1\text{S}_0 \rightarrow ^1\text{P}_1$ transition at a wavelength of $\lambda \approx 399\text{ nm}$, with a natural linewidth of $\Gamma \approx 2\pi \times 29\text{ MHz}$. This broad linewidth is well suited for decelerating atoms emerging from a thermal source at temperatures around 350°C or higher. A Zeeman slower, based on a single laser beam and a spatially varying magnetic field, is commonly used to reduce the longitudinal velocity of the atoms. Alternatively, a 2D MOT can provide transverse cooling and collimation. In both cases, radiation pressure combined with magnetic forces slows the atoms for subsequent capture.

These slowed atoms are loaded into a blue three-dimensional (3D) MOT operating on the $\lambda \approx 399\text{ nm}$ transition [131]. Although the wavelength of 399 nm technically falls within the ultraviolet spectral range, it is sometimes referred to as a “violet MOT” in the literature [146]. However, the majority of sources refer to this trapping phase as a “blue MOT,” a convention we adopt in this work. Due to the large linewidth, the blue MOT features a high capture velocity, making it effective for loading atoms from high-temperature sources. To achieve lower temperatures, the atoms are transferred into a second-stage “green MOT” based on the narrow intercombination line $^1\text{S}_0 \rightarrow ^3\text{P}_1$ at $\lambda \approx 556\text{ nm}$, with a linewidth of $\Gamma \approx 2\pi \times 182\text{ kHz}$. This allows Doppler cooling to the microkelvin regime. Due to the difference in linewidth between the two cooling transitions, the magnetic field gradient must be adjusted between the MOT stages. The narrower green MOT requires much smaller gradients than the blue MOT to avoid excessive Zeeman shifts that would push atoms out of resonance. As a result, the MOT coil current is typically ramped down during the transition from the blue to the green MOT.

In ytterbium, the $^1\text{D}_2$ state lies higher in energy than the $^1\text{P}_1$ state, unlike in strontium where the $^1\text{D}_2$ state is lower [5]. As a result, decay from the $^1\text{P}_1$ state predominantly returns to the ground state [131], enabling efficient accumulation of atoms in the MOT without the need for repumping lasers to load and maintain a large atom number.

The relatively broad linewidth of the intercombination transition compared to strontium (182 kHz versus 7.5 kHz [5]) allows direct loading of the green MOT from a Zeeman-slowed atomic beam, where typically frequency broadening is used to increase the capture velocity [147–149]. Moreover, core-shell MOT configurations can enhance loading rates [150]. Direct loading from an oven into a blue MOT, bypassing both Zeeman slowers and 2D MOTs was also demonstrated using Yb [151].

6. INTERACTION WITH ELECTRIC FIELDS

The interaction between an atom and an external electric field underpins both static energy shifts and coherent optical manipulations in modern atomic-physics experiments. We first derive the DC Stark effect, separating the induced energy shift into scalar, vector, and tensor contributions based on the atomic polarizability in a static field. These shifts give rise to state-dependent optical dipole potentials and define special operating wavelengths, the so-called “magic,” “anti-magic,” and “tune-out” wavelengths. Finally, we address the dynamic response of the atom to near-resonant light, deriving the Rabi frequency that governs coherent population oscillations under the rotating-wave approximation.

6.1. Polarizability

In its most general form, the interaction Hamiltonian between an atom and a classical electric field is

$$H_E = -\hat{\mathbf{d}} \cdot \mathbf{E}, \quad (61)$$

where $\hat{\mathbf{d}}$ is the electric dipole operator and \mathbf{E} is the applied field. We choose the quantization axis along the z -direction, and assume that this interaction Hamiltonian does not mix states any further than described in Section 4.3, so that F and m_F remain good quantum numbers. Far from resonance, the components of the dipole operator are related to the electric field via [143]

$$d_\mu(\mathbf{r}) = \sum_{\nu=x,y,z} \alpha_{\mu\nu}(\omega) E_\nu(\mathbf{r}). \quad (62)$$

Here, we explicitly denote positional dependence and

$$\alpha_{\mu\nu}(\omega) = \Re\{\alpha_{\mu\nu}(\omega)\} + i\Im\{\alpha_{\mu\nu}(\omega)\} \quad (63)$$

is the (complex) dynamic polarizability tensor at angular frequency ω . The real part $\Re\{\alpha_{\mu\nu}(\omega)\}$ relates to the energy shift, while the imaginary part $\Im\{\alpha_{\mu\nu}(\omega)\}$ accounts for absorption and scattering. Hence, the resulting (time-averaged) energy shift for a state $|i\rangle = |F, m_F\rangle$ can be written as [152]

$$V_{\text{ac}}^i(\mathbf{r}; \omega) \equiv \langle i | H_E | i \rangle = -\alpha_{\text{tot}}^i(\omega) \frac{I(\mathbf{r})}{2c\epsilon_0}, \quad (64)$$

where $I(\mathbf{r}) = \frac{1}{2}c\epsilon_0|E(\mathbf{r})|^2$ is the time-averaged local light intensity. The dynamic polarizability $\alpha_{\text{tot}}^i(\omega)$ can be related to the irreducible parts of the polarizability tensor $\alpha_{\mu\nu}$ so that it can be expressed as a sum of contributions from the scalar, vector, and tensor parts [153, 154]

$$\alpha_{\text{tot}}^i(\omega) = \underbrace{\alpha_s^i(\omega)}_{\text{scalar}} + \underbrace{\alpha_v^i(\omega) \sin(2\gamma) \frac{m_F}{2F}}_{\text{vector}} + \underbrace{\alpha_t^i(\omega) \frac{3m_F^2 - F(F+1)}{2F(2F-1)} (3\cos^2\beta - 1)}_{\text{tensor}}, \quad (65)$$

where γ is the ellipticity angle of the light polarization and $\cos(\beta)$ is the angle between \mathbf{E} and the quantization axis. In the generalized form of the polarizability, it is necessary to include the contribution of multiple transitions as well as the frequency of the electric field, ω . The scalar polarizability of the atomic state $|i\rangle$ does not depend on its quantum number m_F and is

$$\alpha_s^i(\omega) = \frac{2}{\hbar} \cdot \frac{1}{3(2F+1)} \sum_{F'} \frac{|\langle F || \mathbf{d} || F' \rangle_R|^2 \omega_{F'F}}{\omega_{F'F}^2 - \omega^2}, \quad (66)$$

where $\langle F || \mathbf{d} || F' \rangle_R$ is the reduced electric dipole matrix element² and $\hbar\omega_{F'F} = E_{F'} - E_F$ is the energy difference between the excited state $|F'\rangle$ and the initial state $|F\rangle$ (see Eq. (14)). The sum runs over all dipole-allowed transitions to states $|F'\rangle$. The vector polarizability is given by

$$\alpha_v^i(\omega) = -\frac{2}{\hbar} \sqrt{\frac{6F}{(F+1)(2F+1)}} \sum_{F'} (-1)^{F+F'} \left\{ \begin{matrix} 1 & 1 & 1 \\ F & F' & F \end{matrix} \right\} \frac{|\langle F || \mathbf{d} || F' \rangle_R|^2 \omega}{\omega_{F'F}^2 - \omega^2}, \quad (67)$$

where the curly brackets are the Wigner 6-j symbols as before. Finally, the tensor polarizability is

$$\alpha_t^i(\omega) = \frac{2}{\hbar} \sqrt{\frac{10F(2F-1)}{3(F+1)(2F+1)(2F+3)}} \sum_{F'} (-1)^{F+F'} \left\{ \begin{matrix} 1 & 2 & 1 \\ F & F' & F \end{matrix} \right\} \frac{|\langle F || \mathbf{d} || F' \rangle_R|^2 \omega_{F'F}}{\omega_{F'F}^2 - \omega^2}. \quad (68)$$

The static polarizability can be found by setting $\omega = 0$.

The reduced hyperfine matrix element $\langle F || \mathbf{d} || F' \rangle_R$ can be further simplified, leaving a reduced matrix element involving only the fine-structure quantum numbers J and J' [143]

$$\langle F || \mathbf{d} || F' \rangle_R = \langle J || \mathbf{d} || J' \rangle_R (-1)^{F'+J+I+1} \sqrt{(2F'+1)(2F+1)} \left\{ \begin{matrix} J & J' & 1 \\ F' & F & I \end{matrix} \right\}. \quad (69)$$

Recall that the reduced matrix elements $\langle J || \mathbf{d} || J' \rangle_R$ are listed in Tables 8 to 14 for the transitions considered in this reference. A special case is provided by stretched hyperfine states, which are a single uncoupled product state of their electronic and nuclear components, $|F = J + I, m_F = \pm F\rangle = |J, m_J = \pm J\rangle \otimes |I, m_I = \pm I\rangle$, so that the light shift (and hence the magic condition) is set by the electronic component $m_J = \pm J$ rather than by hyperfine mixing. Provided the light-shift operator is effectively nuclear-spin independent and diagonal in $|J, m_J\rangle$ for the experimental geometry (so that hyperfine-dependent corrections are negligible), the corresponding stretched-state polarizabilities match across all isotopes to within small residual effects from isotope shifts and hyperfine-resolved intermediate-state structure [155].

Figure 4 shows the dynamic polarizability of the 1S_0 and 3P_0 states. Here, α_{tot} is evaluated using the semi-empirical model described in Refs. [156, 157]. Rather than summing over all allowed transitions, which requires precise knowledge of a variety of highly excited states, the shortest-wavelength transitions are absorbed through a coarse-graining procedure. For 1S_0 this entails a frequency-independent contribution to the polarizability. For 3P_0

² In the Racah convention, polarizability expressions are invariant under the interchange of states since its conjugation rule is $\langle F' || \mathbf{d} || F \rangle_R = (-1)^{F'-F} \langle F || \mathbf{d} || F' \rangle_R^*$ [143].

these transitions are instead captured by a single, *effective* transition. The frequency and linewidth of this effective transition, as well as the polarizability offset for 1S_0 are fitted to reproduce known state-(in)dependent wavelengths, discussed below. The polarizability is stated in atomic units (a.u.), which can be converted to SI through

$$\alpha[\text{A}^2\text{s}^4/\text{kg}] = \frac{m_e e^2 a_0^4}{\hbar^2} \alpha[\text{a.u.}] , \quad (70)$$

or directly into light shift as

$$V_{\text{ac}}[h \text{ Hz}/(\text{W}/\text{cm}^2)] = -\frac{2\pi^2 m_e e^2 a_0^4}{c \epsilon_0 \hbar^3} \times 10^4 \alpha[\text{a.u.}] \approx -0.0469 \alpha[\text{a.u.}] . \quad (71)$$

6.2. State-(in)dependent potentials

The optical dipole potential U experienced by an atom in a light field with optical frequency ω is given, in the far-off-resonant, low-saturation limit, by Eq. (64). A positive (negative) total polarizability produces an attractive (repulsive) potential. At certain “special” wavelengths the polarizabilities of two states satisfy particular relations, giving rise to state-(in)dependent potentials:

- A *magic wavelength* λ_m is defined by

$$\alpha_{\text{tot}}^g(\omega_m) = \alpha_{\text{tot}}^e(\omega_m) ,$$

so that ground (g) and excited (e) states experience identical potentials. This cancels differential Stark shifts and preserves the unperturbed transition frequency.

- An *anti-magic wavelength* λ_a satisfies

$$\alpha_{\text{tot}}^g(\omega_a) = -\alpha_{\text{tot}}^e(\omega_a) ,$$

so that the ground- and excited-state dipole potentials have equal magnitude but opposite sign, $U_g(\mathbf{r}) = -U_e(\mathbf{r})$.

- A *tune-out wavelength* λ_t occurs when the polarizability of one state vanishes:

$$\alpha_{\text{tot}}^g(\omega_t^g) = 0 \quad \text{or} \quad \alpha_{\text{tot}}^e(\omega_t^e) = 0 .$$

At λ_t , an atom in one internal state experiences no optical potential while in the other it remains subject to one, enabling state-selective mobility and precise tunneling control.

Values for magic, anti-magic, and tune-out wavelengths have been theoretically calculated in, e.g., Refs. [8, 157–159]. Table 7 presents experimentally measured magic and tune-out wavelengths for ^{171}Yb . We note that measurements using ^{174}Yb are included for wavelengths where hyperfine effects play a negligible role, i.e., those involving solely 1S_0 and/or 3P_0 , as well as stretched states (see the discussion above). Special wavelengths measured in ^{174}Yb for these states can be used for ^{171}Yb at the level of accuracy relevant for Table 7. All values inferred from ^{174}Yb are indicated with an asterisk. We also note additional observations of (nearly) magic wavelengths for other transitions of ^{174}Yb in Refs. [54, 160–163].

The following comments apply, as pertaining to Table 7:

- The ~ 759 nm magic wavelength for the $^1S_0 \rightarrow ^3P_0$ transition has been extensively studied because of its importance to optical lattice clocks. Various results have been obtained [84, 88, 90, 91, 94, 111–113, 115–117, 119, 164–168], and isotope shifts can be inferred by comparison to measurements of the magic wavelength in other isotopes [93]. We note that these references frequently contain the *operational* magic wavelength, which is subtly different from the electric dipole (E1) magic wavelength, see, e.g., Ref. [94] for an extended discussion. Nonetheless, we simply report in Table 7 the average of all results listed in the references above. The stated angle of $\sim 17^\circ$ only applies to the triple-magic condition including 3P_1 , since 1S_0 and 3P_0 have no tensor polarizability and hence realize the magic condition under any angle.
- Ref. [62] does not specify the angle between quantization axis and polarization of the light used to observe the magic condition for the $^1S_0 \rightarrow ^3P_1$ $|F' = 3/2, m_{F'} = \pm 1/2\rangle$ transition.

- For the magic wavelength reported in Ref. [169] we were likewise unable to retrieve the angle for which this magic condition was achieved. Additionally, it highlights that the stated number is an *operational* magic wavelength, and that due to its proximity to the $^3P_1 \rightarrow ^1D_2$ transition the precise magic condition depends on residual broadband content of the laser light.
- The last column lists the polarizability of the 1S_0 state at each wavelength, calculated using the semi-empirical model described above.

6.3. Calculation of Rabi Frequencies

Consider an atom with a ground-state manifold $|g\rangle = |F_g, m_{F_g}\rangle$ and an excited-state manifold $|e\rangle = |F_e, m_{F_e}\rangle$. A near-resonant laser with an angular frequency ω_L drives the $|g\rangle \leftrightarrow |e\rangle$ transition via the electric-dipole Hamiltonian:

$$H_{\text{int}}(t) = -\hat{\mathbf{d}} \cdot \mathbf{E}(t) \approx -\langle e|\hat{\mathbf{d}} \cdot \hat{\mathbf{e}}_q|g\rangle E_0 \cos(\omega_L t) (|e\rangle \langle g| + |g\rangle \langle e|), \quad (72)$$

where $\langle e|\hat{\mathbf{d}} \cdot \hat{\mathbf{e}}_q|g\rangle$ is the matrix element of the dipole operator between the two levels, including the polarization component. Here, q labels the spherical polarization component. $q = 0$ corresponds to π -polarization, i.e., electric field along the quantization axis, while $q = +1$ and $q = -1$ correspond to right-circular σ^+ and left-circular σ^- polarization, respectively. Under the rotating-wave approximation, the Rabi frequency $\Omega_q^{g \rightarrow e}$ is

$$\Omega_q^{g \rightarrow e} = \frac{1}{\hbar} \langle e|\hat{\mathbf{d}} \cdot \hat{\mathbf{e}}_q|g\rangle E_0. \quad (73)$$

This matrix element can be reduced using the Wigner-Eckart theorem [143]

$$\langle F_g m_{F_g} | d_q | F_e m_{F_e} \rangle = \frac{\langle F_g \| \mathbf{d} \| F_e \rangle_R}{\sqrt{2F_g + 1}} \langle F_g m_{F_g} | F_e m_{F_e}; 1q \rangle, \quad (74)$$

separating it into a product of a reduced dipole matrix element which depends on F_g and F_e but not on m_{F_g} or m_{F_e} , and a Clebsch–Gordan factor that accounts for the coupling between the specific Zeeman sublevels (m_{F_g} , m_{F_e}) under polarization q . The Clebsch–Gordan coefficient can be calculated using the Wigner 3- j symbol as [143]

$$\langle F_g m_{F_g} | F_e m_{F_e}; 1q \rangle = \langle F_e m_{F_e}; 1q | F_g m_{F_g} \rangle = \sqrt{2F_g + 1} (-1)^{F_e - 1 + m_{F_g}} \begin{pmatrix} F_e & 1 & F_g \\ m_{F_e} & q & -m_{F_g} \end{pmatrix}. \quad (75)$$

This separation greatly simplifies practical calculations, since all the dependence on magnetic quantum numbers and polarization is contained in the known tabulated Clebsch–Gordan factor. Further, using Eq. (69), the matrix element between hyperfine substates can be related to the reduced matrix elements tabulated in Tables 8 to 14. Explicitly, this gives

$$\langle F_g m_{F_g} | d_q | F_e m_{F_e} \rangle = (-1)^{2F_e + J_g + I + m_{F_g}} \sqrt{(2F_g + 1)(2F_e + 1)} \begin{pmatrix} F_e & 1 & F_g \\ m_{F_e} & q & -m_{F_g} \end{pmatrix} \left\{ \begin{matrix} J_g & J_e & 1 \\ F_e & F_g & I \end{matrix} \right\} \langle J_g \| \mathbf{d} \| J_e \rangle_R \quad (76)$$

$$\equiv w_q^{g \rightarrow e} \langle J_g \| \mathbf{d} \| J_e \rangle_R. \quad (77)$$

The values of the factor $w_q^{g \rightarrow e}$ for various transitions can be found in Figs. 5 to 7. Substituting into Eq. (73) yields the (real, positive) Rabi frequency

$$\Omega_q^{g \rightarrow e} = |w_q^{g \rightarrow e}| \frac{|\langle J_g \| \hat{\mathbf{d}} \| J_e \rangle_R|}{\hbar} E_0. \quad (78)$$

We consider an atom driven by a Gaussian laser beam, whose waist is much larger than the spatial extent of the atomic wavefunction. In this case, the atom experiences the peak intensity of the Gaussian beam, given by

$$I_0 = \frac{2P}{\pi w_0^2} = \frac{8P}{\pi D^2}, \quad (79)$$

where P is the total optical power and w_0 is the $1/e^2$ beam radius so that the full $1/e^2$ diameter is $D = 2w_0$. Using Eq. (91), the peak electric-field amplitude is

$$I_0 = \frac{1}{2} c \varepsilon_0 E_0^2 \implies E_0 = \sqrt{\frac{2I_0}{\varepsilon_0 c}} = \sqrt{\frac{16P}{\varepsilon_0 c \pi D^2}}. \quad (80)$$

Using the separated form of the Rabi frequency (see Eq. (78)) together with the peak electric-field amplitude (see Eq. (80)), we find

$$\Omega_q^{g \rightarrow e} = |w_q^{g \rightarrow e}| \frac{|\langle J_g || \hat{\mathbf{d}} || J_e \rangle_R|}{\hbar} \sqrt{\frac{16P}{\varepsilon_0 c \pi D^2}}. \quad (81)$$

In Table 8-14, we list numerical values of $\Omega_q^{g \rightarrow e}$ obtained from Eq. (81) under the following common experimental parameters: a laser power of $P = 1$ mW with a Gaussian beam diameter of $D = 1$ mm, and π -polarization ($q = 0$). Specifically, we calculate the Rabi frequency for $|F_g, m_{F_g}\rangle \rightarrow |F_e, m_{F_e}\rangle$ transitions as specified.

7. RESONANCE FLUORESCENCE

In this Section, we analyze the interaction of a two-level atom with a monochromatic classical electromagnetic field. Under the electric-dipole and rotating-wave approximations, the atom behaves as an ideal two-level system whose dynamics are governed by the optical Bloch equations. We derive these equations, solve for the steady-state excited-state population, and then obtain expressions for the total photon scattering rate, the saturation intensity, and the on-resonance scattering cross section.

7.1. Optical Bloch Equations

Consider an atom with ground state $|g\rangle$ and excited state $|e\rangle$, separated by an energy $\hbar\omega_0$. We drive the $|g\rangle \leftrightarrow |e\rangle$ transition with a classical, linearly polarized, monochromatic field of the form

$$\mathbf{E}(t) = E_0 \hat{\mathbf{e}} \cos(\omega_L t), \quad (82)$$

where E_0 is the real field amplitude, $\hat{\mathbf{e}}$ is the unit polarization vector, and ω_L is the laser frequency. The atom–field interaction Hamiltonian in the electric-dipole approximation is

$$H_{\text{int}} = -\hat{\mathbf{d}} \cdot \mathbf{E}(t) = -(d\hat{\sigma}_+ + d^*\hat{\sigma}_-) E_0 \cos(\omega_L t), \quad (83)$$

where $\hat{\mathbf{d}}$ is the atomic dipole moment, $d = \langle e | \hat{\mathbf{d}} \cdot \hat{\mathbf{e}} | g \rangle$ is the (complex) dipole matrix element, and $\hat{\sigma}_- = |g\rangle \langle e|$ (with $\hat{\sigma}_+ = \hat{\sigma}_-^\dagger$) is the lowering operator for the two-level system. We define the Rabi frequency as

$$\Omega = \frac{d E_0}{\hbar}. \quad (84)$$

We move into a frame rotating at the laser frequency ω_L and apply the rotating-wave approximation (RWA). Then, the density operator ρ of the two-level atom is described by the optical Bloch equations [4]

$$\dot{\rho}_{gg} = \frac{i\Omega}{2}(\rho_{eg} - \rho_{ge}) + \Gamma \rho_{ee}, \quad (85a)$$

$$\dot{\rho}_{ee} = -\frac{i\Omega}{2}(\rho_{eg} - \rho_{ge}) - \Gamma \rho_{ee}, \quad (85b)$$

$$\dot{\rho}_{ge} = -(\gamma + i\Delta) \rho_{ge} - \frac{i\Omega}{2}(\rho_{ee} - \rho_{gg}), \quad (85c)$$

where $\rho_{ij} = \langle i | \rho | j \rangle$ are the matrix elements of the density operator in the $\{|g\rangle, |e\rangle\}$ basis, $\gamma = \frac{\Gamma}{2} + \gamma_c$ is the total coherence-decay (“transverse”) rate, with γ_c a pure-dephasing rate (e.g., due to collisions), and $\Delta = \omega_L - \omega_0$ is the detuning of the driving field from atomic resonance. In writing Eq. (85), we have neglected any additional couplings to auxiliary levels or motional effects. The term $\Gamma \rho_{ee}$ in the population equations accounts for radiative decay from $|e\rangle$ to $|g\rangle$, while the coherence ρ_{ge} and its conjugate $\rho_{eg} = \rho_{ge}^*$ evolve under both dephasing and the coherent drive Ω .

7.2. Steady-State Excited-State Population

Here, we are primarily interested in the long-time (steady-state) solution, where $\dot{\rho}_{ij} = 0$ for all i, j . In the steady state and assuming the purely radiative case ($\gamma = \Gamma/2$, i.e., $\gamma_c = 0$), one finds

$$\rho_{ee}^{(\infty)} = \frac{\left(\frac{\Omega}{\Gamma}\right)^2}{1 + 4\left(\frac{\Delta}{\Gamma}\right)^2 + 2\left(\frac{\Omega}{\Gamma}\right)^2}. \quad (86)$$

We can rewrite this equation

$$\rho_{ee}^{(\infty)} = \frac{s/2}{1 + s + 4(\Delta/\Gamma)^2}, \quad (87)$$

where s is the on-resonance saturation parameter, given by

$$s = \frac{2\Omega^2}{\Gamma^2}. \quad (88)$$

Equation (86) shows that, on resonance ($\Delta = 0$), the excited-state population saturates to $1/2$ when $\Omega \gg \Gamma$.

7.3. Total Photon Scattering Rate

The total photon scattering (or fluorescence) rate is the rate at which population decays from the excited state, given by

$$R_{\text{sc}} = \Gamma \rho_{ee}. \quad (89)$$

In the steady state, we find

$$R_{\text{sc}} = \Gamma \rho_{ee}^{(\infty)} = \frac{\Gamma}{2} \frac{s}{1 + s + 4(\Delta/\Gamma)^2}, \quad (90)$$

where we have set $s = 2\Omega^2/\Gamma^2$ as above. Rewriting Eq. (90) in terms of the incident intensity I leads naturally to the definition of the saturation intensity I_{sat} .

7.4. Saturation Intensity

The average intensity of a plane electromagnetic wave in free space is

$$I = \frac{1}{2} c \varepsilon_0 E_0^2, \quad (91)$$

where c is the speed of light and ε_0 is the vacuum permittivity. In terms of the Rabi frequency (see Eq. (84)), one finds

$$I = \frac{1}{2} c \varepsilon_0 \left(\hbar \frac{\Omega}{|d|} \right)^2 = \frac{c \varepsilon_0 \hbar^2}{2|d|^2} \Omega^2. \quad (92)$$

We define the (on-resonance) saturation intensity I_{sat} using the condition that $s = 1$ when $I = I_{\text{sat}}$. Since $s = 2\Omega^2/\Gamma^2$, setting $s = 1$ yields

$$I_{\text{sat}} = \frac{c \varepsilon_0 \hbar^2}{2|d|^2} \frac{\Gamma^2}{2} = \frac{c \varepsilon_0 \hbar^2 \Gamma^2}{4|d|^2}. \quad (93)$$

Using Eq. (51), we find the saturation intensity for a cycling transition

$$I_{\text{sat}} = \frac{\hbar \omega_0^3 \Gamma}{12\pi c^2} = \frac{\pi \hbar c \Gamma}{3 \lambda^3}. \quad (94)$$

Equivalently, I_{sat} and Ω are often defined as

$$\frac{I}{I_{\text{sat}}} = \frac{2\Omega^2}{\Gamma^2} = s \implies \Omega = \frac{\Gamma}{\sqrt{2}} \sqrt{\frac{I}{I_{\text{sat}}}}. \quad (95)$$

Using this definition of I_{sat} , we can write the scattering rate (see Eq. (90)) as

$$R_{\text{sc}} = \left(\frac{\Gamma}{2} \right) \frac{\left(\frac{I}{I_{\text{sat}}} \right)}{1 + 4 \left(\frac{\Delta}{\Gamma} \right)^2 + \left(\frac{I}{I_{\text{sat}}} \right)}. \quad (96)$$

When the laser is exactly on resonance ($\Delta = 0$), the scattering rate reduces to

$$R_{\text{sc}}(\Delta = 0) = \frac{\Gamma}{2} \frac{I/I_{\text{sat}}}{1 + I/I_{\text{sat}}} . \quad (97)$$

Thus, on resonance, the scattering rate on a fully saturated transition ($I \gg I_{\text{sat}}$) approaches $\Gamma/2$, consistent with the fact that at saturation $\rho_{ee}^{(\infty)} \rightarrow 1/2$.

7.5. On-Resonance Scattering Cross Section

It is often convenient to express the scattering properties in terms of an effective cross section $\sigma(\Delta, I)$, defined as the power radiated by the atom divided by the incident energy flux so that the power scattered by the atom is $\sigma(\Delta, I)I$. Using Eq. (96), we can calculate the scattering cross section as

$$R_{\text{sc}} = \sigma(\Delta, I)I \implies \sigma(\Delta, I) = \frac{R_{\text{sc}}}{I} = \frac{\Gamma}{2I} \frac{I/I_{\text{sat}}}{1 + I/I_{\text{sat}} + 4(\Delta/\Gamma)^2} . \quad (98)$$

We define the low-intensity on-resonance cross section as

$$\sigma_0 = \frac{\hbar\omega_0 \Gamma}{2I_{\text{sat}}} . \quad (99)$$

For a cycling transition, this reduces to [64]

$$\sigma_0 = \frac{3\lambda^2}{2\pi} . \quad (100)$$

Then, we can write the scattering cross section as

$$\sigma(\Delta, I) = \frac{\sigma_0}{1 + 4(\Delta/\Gamma)^2 + I/I_{\text{sat}}} . \quad (101)$$

On resonance ($\Delta = 0$), this reduces to

$$\sigma(0, I) = \frac{\sigma_0}{1 + I/I_{\text{sat}}} , \quad (102)$$

showing that at $I = I_{\text{sat}}$ the scattering cross section is half of its low-intensity value σ_0 .

8. DATA TABLES

Table 1: Fundamental Physical Constants (2022 CODATA recommended values) [15].

Constant	Symbol	Value
Speed of Light	c	$2.997\,924\,58 \times 10^8$ m/s (exact)
Permeability of Vacuum	μ_0	$1.256\,637\,061\,27(20) \times 10^{-6}$ N/A ²
Permittivity of Vacuum	ϵ_0	$(\mu_0 c^2)^{-1} \approx 8.854\,187\,818\,8(14) \times 10^{-12}$ F/m
Planck's Constant	h	$6.626\,070\,15 \times 10^{-34}$ J s (exact)
Reduced Planck Constant	\hbar	$\sim 1.054\,571\,817 \times 10^{-34}$ J s
Elementary Charge	e	$1.602\,176\,634 \times 10^{-19}$ C (exact)
Bohr Magneton	μ_B	$9.274\,010\,065\,7(29) \times 10^{-24}$ J/T
Nuclear Magneton	μ_N	$5.050\,783\,739\,3(16) \times 10^{-27}$ J/T
Atomic Mass Unit	u	$1.660\,539\,068\,92(52) \times 10^{-27}$ kg
Electron Mass	m_e	$9.109\,383\,713\,9(28) \times 10^{-31}$ kg
Bohr Radius	a_0	$5.291\,772\,105\,44(82) \times 10^{-11}$ m
Boltzmann Constant	k_B	$1.380\,649 \times 10^{-23}$ J/K (exact)

Table 2: Physical properties of ¹⁷¹Yb.

Property	Symbol	Value	Reference
Atomic Number	Z	70	
Total Nucleons	$Z + N$	171	
Nuclear Spin	I	1/2	
Particle Statistics		fermionic	
Relative Natural Abundance	η	14.239(5) %	[17]
Nuclear Lifetime	τ_n	stable	
Atomic Mass	m	170.936 331 515(14) u $2.838\,464\,567\,8(9) \times 10^{-25}$ kg	[16]
RMS Nuclear Charge Radius	R	5.2906(57) fm	[170]
Electron Spin g-Factor	g_S	2.002 319 304 360 92(36)	[15]
Electron Orbital g-Factor	g_L	$\sim 0.999\,996\,79$	
Nuclear Magnetic Moment	μ	0.4923(4) μ_N	[73]
Nuclear Spin g-Factor	g_I	-0.000 536 2(4)	
Density at 20 °C	ρ_m	6904(2) kg/m ³	[19]
Molar Volume at 20 °C	V_m	25.066(7) cm ³ /mol	[19]
Melting Point	T_M	1097 K (824 °C)	[12]
Boiling Point	T_B	1496 K (1196 °C)	[12]
Specific Heat Capacity	c_p	0.155 J/(g K)	[12]
Molar Heat Capacity	C_p	26.74 J/(mol K)	[12]
Vapor Pressure at 25 °C	P	$1.69(8) \times 10^{-16}$ Pa $1.27(6) \times 10^{-18}$ Torr	[20]
Ionization Energy	E_I	50 443.0676(12) cm ⁻¹ 6.254 143 30(15) eV R_B : 4.7	[21–29]
	E_I^0	50 442.795 744 cm ⁻¹	[63]
	E_I^1	50 443.217 463 cm ⁻¹	[63]
Ionic hyperfine constant	$A_{\text{hfs}}(6s^2S_{1/2})$	12.642 812 124 2(12) GHz	[71]

Table 3: Relative natural abundance, mass, and nuclear spin of all stable ytterbium isotopes. All values are from Refs. [16, 17].

Isotope	Relative Natural Abundance (%)	Atomic Mass (u)	Nuclear Spin I
^{168}Yb	0.126 48(22)	167.933 891 30(10)	0
^{170}Yb	3.0280(19)	169.934 767 243(11)	0
^{171}Yb	14.239(5)	170.936 331 515(14)	1/2
^{172}Yb	21.789(5)	171.936 386 654(15)	0
^{173}Yb	16.119(3)	172.938 216 212(12)	5/2
^{174}Yb	31.881(8)	173.938 867 546(12)	0
^{176}Yb	12.817(12)	175.942 574 706(16)	0

Table 4: Scattering lengths between the ytterbium isotopes, given in units of a_0 . All values are calculated with a contribution from Ref. [36] plus additional references if indicated.

	^{168}Yb	^{170}Yb	^{171}Yb	^{172}Yb	^{173}Yb	^{174}Yb	^{176}Yb
^{168}Yb	252.86(6) [35]	117.268(10) [35]	89.2(17)	65.117(8) [35]	38.6(25)	2.599(24) [35]	-357.1(6) [35]
^{170}Yb		63.957(8) [35, 37]	36.5(25)	-1.916(27) [35]	-81(7)	-512.7(11) [35]	209.69(5) [35]
^{171}Yb			-3(4)	-84(7)	-580(60)	429(13)	141.5(15)
^{172}Yb				-592.3(14) [35]	418(13)	200.82(4) [35]	106.310(11) [35]
^{173}Yb					$^{199}(5)$ $R_B: 2.3$ [38]	138.7(15)	79.7(19)
^{174}Yb						105.037(11) [35, 39, 40]	54.573(18) [35]
^{176}Yb							-24.06(9) [35]

Table 5: Landé g_J factor, linear Zeeman coefficient, and hyperfine structure constant A_{hfs} for selected states of ^{171}Yb . Asterisks denote theoretical values.

State	F	g_J	$\mu_B g_F / h$ (kHz/G)	Ref.	A_{hfs} / h (MHz)	Ref.
$^1\text{S}_0$	1/2	-	-0.7505(6)	[73]	0	-
$^1\text{P}_1$	1/2	1.035(5)	1932(9)	[171]	-214.06(17)	[65–67, 172–179]
	3/2		965(5)		$R_B: 3.3$	
$^3\text{P}_0$	1/2	-	-1.1496(6)	[49, 50, 83, 84]	0	-
$^3\text{P}_1$	1/2	1.492 820(31)	2786.10(6)	[171, 180]	3957.85(5)	[127, 128, 181–189]
	3/2		1392.674(29)		$R_B: 2.6$	
$^3\text{P}_2$	3/2	1.501*	~ 2521	-	2680.9(20)	[190–193]
	5/2		~ 1681		$R_B: 6.3$	
$^3\text{D}_1$	1/2	0.499*	~ 931	-	-2038.30(11)	[69, 85, 86, 194, 195]
	3/2		~ 465		$R_B: 1.0$	
$^3\text{D}_2$	3/2	1.167*	~ 1960	-	1313.8(33)	[68, 69]
	5/2		~ 1307			
$^3\text{S}_1$	1/2	2.01(1)	3751(19)	[196]	6838.41(26)	[177, 190, 192, 197–199]
	3/2		1875(9)		$R_B: 3.1$	

Table 6: Isotope shifts in MHz for selected states, relative to 1S_0 and compared to ^{174}Yb .

State	^{168}Yb	^{170}Yb	^{171}Yb
1P_1	1887.64(23) $R_B: 5.0$ [65, 66, 106, 172–174, 176]	1187.8(27) $R_B: 47.2$ [65, 66, 104–106, 172–176, 179, 200]	940.8(9) $R_B: 26.8$ [65, 66, 104–106, 172, 173, 175, 176, 179, 201]
3P_0	3626.971 068 8(29) [87]	2268.486 592 6(19) [87]	1811.281 647 3(10) [87, 91]
3P_1	3655.88(20) $R_B: 3.6$ [127, 128, 182, 184–187, 202]	2286.55(5) $R_B: 1.3$ [67, 127, 128, 182–187, 202]	1826.88(19) $R_B: 5.8$ [67, 127, 128, 182–187, 202]
3P_2	3677.546 251(7) [163]	2300.235 712(6) [163]	?
3D_1	?	2542(12) $R_B: 8.1$ [69, 194]	2038.9(12) $R_B: 2.0$ [69, 194]
3D_2	?	2531(5) [69]	2019(6) [69]
3S_1	2100(8) $R_B: 3.5$ [186, 192]	1321.2(1) $R_B: 4.1$ [123, 177, 186, 192, 197, 198]	1057.34(15) [123, 177, 198]

Table 6 (*continued*): Isotope shifts in MHz for selected states, relative to 1S_0 and compared to ^{174}Yb .

State	^{172}Yb	^{173}Yb	^{176}Yb
1P_1	532.95(34) $R_B: 8.0$ [65, 66, 104–106, 172–175, 179, 200, 201]	291.51(5) [65, 104, 172, 173, 179]	−509.25(7) $R_B: 1.7$ [65, 66, 104–106, 172–175, 179, 200, 201]
3P_0	992.714 586 6(21) [87]	551.536 050(10) [203]	−946.921 774 9(29) [87]
3P_1	1000.73(8) $R_B: 3.0$ [67, 127, 128, 182–187, 202]	556.23(16) $R_B: 3.5$ [67, 127, 128, 182–187, 202]	−954.69(4) $R_B: 1.9$ [67, 127, 128, 182–187, 202]
3P_2	1006.735 628(5) [163]	?	−960.303 321(7) [163]
3D_1	1112(8) $R_B: 11.5$ [69, 194]	619.4(8) $R_B: 1.3$ [69, 194]	−1063(6) $R_B: 9.5$ [69, 194]
3D_2	1100(4) [69]	609(6) [69]	−1059(11) [69]
3S_1	579.0(19) $R_B: 13.1$ [123, 177, 186, 192, 197, 198]	320.97(12) [123, 177, 198]	−543.1(29) $R_B: 19.2$ [123, 177, 186, 192, 197, 198]

Table 7: Experimentally measured magic and tune-out wavelengths, supplemented with theoretical polarizability values for 1S_0 . Asterisks denote a measurement performed with ^{174}Yb .

Type	Transition	β ($^\circ$)	λ (nm)	$\omega_0/2\pi$ (THz)	Ref.	α_{tot} (a.u.)
magic	$^1S_0 - ^1P_1 F' = 3/2, m_{F'} = \pm 3/2\rangle$	0	$\sim 532^*$	$\sim 564^*$	[204]	258
	$^1S_0 - ^3P_0$	$\forall \angle$	~ 397.634	~ 753.941	[205]	-15 495
		$\forall \angle$	459.5960(5)	652.2956(7)	[156, 206]	469
		$\forall \angle$	552.610 74(19)*	542.502 05(19)*	[156]	57
	$^1S_0 - ^3P_0 - ^3P_1 F' = 3/2, m_{F'} = -1/2\rangle$	~ 17	759.356 063 3(31)	394.798 267 2(16) $R_B: 4.3$	[207], ^a	188
	$^1S_0 - ^3P_1 F' = 3/2, m_{F'} = \pm 1/2\rangle$?	486.78(1)	615.868(13)	[62]	370
		?	1036.13(1)	289.3387(28)	[169]	162
	$^1S_0 - ^3P_1 F' = 3/2, m_{F'} = +3/2\rangle$	90	~ 483	~ 621	[206]	~ 359
		90	~ 783.8	~ 382.5	[208]	~ 184
		0	1036.12(3)*	289.341(8)*	[209]	162
90		1035.83(3)*	289.422(8)*	[209]	162	
tune-out	1S_0	$\forall \angle$	553.2936(5)*	541.8325(5)*	[156]	0
	3P_0	$\forall \angle$	576.613(10)*	519.920(9)*	[162]	277

^a: [84, 88, 90, 91, 94, 111–113, 115–117, 119, 164–168]

Table 8: $^1S_0 \rightarrow ^1P_1$ transition (Zeeman slower, blue MOT).

Parameter	Symbol	Value	Ref.
Frequency	ω_0	$2\pi \times 751.527 471 1(8)$ THz $R_B: 6.3$	[66, 104–106]
Transition Energy	$\hbar\omega_0$	3.108 067 885 6(32) eV	
Wavelength (vacuum)	λ	398.910 844 3(4) nm	
Wavelength (air)	λ_{air}	398.802 070(4) nm	
Wavenumber (vacuum)	$k_L/2\pi$	25 068.258 091(26) cm^{-1}	
Lifetime excited state	τ	5.464(11) ns $R_B: 2.3$	[133, 135, 136, 139, 210–212]
Decay rate	Γ	$183.0(4) \times 10^6 \text{ s}^{-1}$	
Natural Line Width	$\Delta\nu_{\text{FWHM}}$	$2\pi \times 29.13(6)$ MHz	
Branching Ratio	β	$1 - 6(4) \times 10^{-8}$	[132]
Oscillator strength	f	1.3098(27)	
Recoil velocity	v_r	~ 5.852 mm/s	
Recoil energy	ω_r	$\sim 2\pi \times 7.335$ kHz	
Recoil temperature	T_r	~ 704 nK	
Doppler shift ($v = v_r$)	$\Delta\omega_d$	$\sim 2\pi \times 14.670$ kHz	
Doppler Temperature	T_D	699.0(15) μK	
Reduced E1 Matrix Element	$\langle J e r J' \rangle_R$	4.147(4) ea_0	
Saturation Intensity	I_{sat}	59.97(12) mW/cm^2	
Resonant Cross Section	σ_0	$\sim 7.598 \times 10^{-14} \text{ m}^2$	
Rabi Frequency $P = 1 \text{ mW}, D = 1 \text{ mm}$	$\Omega_0^{ \frac{1}{2}, \frac{1}{2}\rangle \rightarrow \frac{3}{2}, \frac{3}{2}\rangle}$	$2\pi \times 42.44(4)$ MHz	

Table 9: $^1S_0 \rightarrow ^3P_0$ transition (yellow clock).

Parameter	Symbol	Value	Ref.
Frequency	ω_0	$2\pi \times 518.295\,836\,590\,863\,63(10)$ THz	[121]
Transition Energy	$\hbar\omega_0$	2.143 499 348 838 961 5(4) eV	
Wavelength (vacuum)	λ	578.419 575 916 162 50(11) nm	
Wavelength (air)	λ_{air}	578.264 935(6) nm	
Wavenumber (vacuum)	$k_L/2\pi$	17 288.488 177 740 069(3) cm^{-1}	
Lifetime excited state	τ	21.0(18) s $R_B: 1.3$	[213, 214]
Decay rate	Γ	0.048(4) s^{-1}	
Natural Line Width	$\Delta\nu_{\text{FWHM}}$	$2\pi \times 7.6(6)$ mHz	
Recoil velocity	v_r	~ 4.036 mm/s	
Recoil energy	ω_r	$\sim 2\pi \times 3.489$ kHz	
Recoil temperature	T_r	~ 335 nK	
Doppler shift ($v = v_r$)	$\Delta\omega_d$	$\sim 2\pi \times 6.977$ kHz	

Table 10: $^1S_0 \rightarrow ^3P_1$ transition (green MOT).

Parameter	Symbol	Value	Ref.
Frequency	ω_0	$2\pi \times 539.388\,426\,84(12)$ THz $R_B: 2.9$	[181, 182, 184]
Transition Energy	$\hbar\omega_0$	2.230 731 293 0(5) eV	
Wavelength (vacuum)	λ	555.800 686 63(13) nm	
Wavelength (air)	λ_{air}	555.651 877(6) nm	
Wavenumber (vacuum)	$k_L/2\pi$	17 992.061 256(4) cm^{-1}	
Lifetime excited state	τ	872.6(19) ns $R_B: 1.2$	[133, 134, 136, 137, 139, 195, 212, 215–218]
Decay rate	Γ	$1.1460(25) \times 10^6$ s^{-1}	
Natural Line Width	$\Delta\nu_{\text{FWHM}}$	$2\pi \times 182.4(4)$ kHz	
Oscillator strength	f	0.015 923(35)	
Recoil velocity	v_r	~ 4.200 mm/s	
Recoil energy	ω_r	$\sim 2\pi \times 3.778$ kHz	
Recoil temperature	T_r	~ 363 nK	
Doppler shift ($v = v_r$)	$\Delta\omega_d$	$\sim 2\pi \times 7.557$ kHz	
Doppler Temperature	T_D	4.377(10) μK	
Reduced E1 Matrix Element	$\langle J er J' \rangle_R$	0.5398(6) ea_0	
Saturation Intensity	I_{sat}	138.85(30) $\mu\text{W}/\text{cm}^2$	
Resonant Cross Section	σ_0	$\sim 1.475 \times 10^{-13}$ m^2	
Rabi Frequency $P = 1$ mW, $D = 1$ mm	$\Omega_0^{ \frac{1}{2}, \frac{1}{2}\rangle \rightarrow \frac{3}{2}, \frac{3}{2}\rangle}$	$2\pi \times 5.523(6)$ MHz	

Table 11: $^1S_0 \rightarrow ^3P_2$ transition (green clock).

Parameter	Symbol	Value	Ref.
Frequency	ω_0	$2\pi \times 590.904\,33(4)$ THz	[123]
Transition Energy	$\hbar\omega_0$	2.443 783 93(17) eV	
Wavelength (vacuum)	λ	507.345 17(4) nm	
Wavelength (air)	λ_{air}	507.208 82(4) nm	
Wavenumber (vacuum)	$k_L/2\pi$	19 710.4467(14) cm^{-1}	
Lifetime excited state	τ	~ 8.9 s	[129]
Decay rate	Γ	~ 0.112 s^{-1}	
Natural Line Width	$\Delta\nu_{\text{FWHM}}$	$\sim 2\pi \times 17.9$ mHz	
Recoil velocity	v_r	~ 4.601 mm/s	
Recoil energy	ω_r	$\sim 2\pi \times 4.535$ kHz	
Recoil temperature	T_r	~ 435 nK	
Doppler shift ($v = v_r$)	$\Delta\omega_d$	$\sim 2\pi \times 9.069$ kHz	

Table 12: $^3P_0 \rightarrow ^3D_1$ transition (infrared repumper for yellow clock).

Parameter	Symbol	Value	Ref.
Frequency	ω_0	$2\pi \times 215.870\,144\,57(9)$ THz	[85, 86, 194]
Transition Energy	$\hbar\omega_0$	0.892 767 183 6(4) eV	
Wavelength (vacuum)	λ	1388.762 946 4(6) nm	
Wavelength (air)	λ_{air}	1388.396 915(14) nm	
Wavenumber (vacuum)	$k_L/2\pi$	7200.652 945 3(29) cm^{-1}	
Lifetime excited state	τ	332(11) ns $R_B: 1.6$	[137, 195]
Decay rate	Γ	$3.01(10) \times 10^6$ s^{-1}	
Natural Line Width	$\Delta\nu_{\text{FWHM}}$	$2\pi \times 479(16)$ kHz	
Branching Ratios	$\beta_{3D1 \rightarrow 3P2}$ $\beta_{3D1 \rightarrow 3P1}$ $\beta_{3D1 \rightarrow 3P0}$	0.0099(39) 0.352(27) 0.638(27)	[132]
Partial decay rate	Γ_{partial}	$1.92(10) \times 10^6$ s^{-1}	
Recoil velocity	v_r	~ 1.681 mm/s	
Recoil energy	ω_r	$\sim 2\pi \times 605.2$ Hz	
Recoil temperature	T_r	~ 58.1 nK	
Doppler shift ($v = v_r$)	$\Delta\omega_d$	$\sim 2\pi \times 1.210$ kHz	
Doppler Temperature	T_D	11.5(4) μK	
Reduced E1 Matrix Element	$\langle J er J' \rangle_R$	2.76(7) ea_0	
Rabi Frequency $P = 1$ mW, $D = 1$ mm	$\Omega_0^{ \frac{1}{2}, \frac{1}{2}\rangle \rightarrow \frac{3}{2}, \frac{3}{2}\rangle}$	$2\pi \times 28.3(8)$ MHz	

Table 13: ${}^3P_0 \rightarrow {}^3S_1$ transition (red repumper for yellow clock).

Parameter	Symbol	Value	Ref.
Frequency	ω_0	$2\pi \times 461.868\,176\,72(22)$ THz	[190, 198]
Transition Energy	$\hbar\omega_0$	1.910 133 298 7(9) eV	
Wavelength (vacuum)	λ	649.086 629 28(31) nm	
Wavelength (air)	λ_{air}	648.913 718(6) nm	
Wavenumber (vacuum)	$k_L/2\pi$	15 406.264 047(7) cm^{-1}	
Lifetime excited state	τ	13.8(17) ns R_B : 1.4	[135, 196]
Decay rate	Γ	$7.2(9) \times 10^7 \text{ s}^{-1}$	
Natural Line Width	$\Delta\nu_{\text{FWHM}}$	$2\pi \times 11.5(14)$ MHz	
Branching Ratios	$\beta_{3S_1 \rightarrow 3P_2}$ $\beta_{3S_1 \rightarrow 3P_1}$ $\beta_{3S_1 \rightarrow 3P_0}$ $\beta_{3S_1 \rightarrow 1P_1}$	0.508(26) 0.360(25) 0.130(13) 0.0021(9)	[132]
Partial decay rate	Γ_{partial}	$9.4(15) \times 10^6/\text{s}$	
Recoil velocity	v_r	~ 3.596 mm/s	
Recoil energy	ω_r	$\sim 2\pi \times 2.770$ kHz	
Recoil temperature	T_r	~ 266 nK	
Doppler shift ($v = v_r$)	$\Delta\omega_d$	$\sim 2\pi \times 5.541$ kHz	
Doppler Temperature	T_D	277(33) μK	
Reduced E1 Matrix Element	$\langle J er J' \rangle_R$	1.96(15) ea_0	
Rabi Frequency $P = 1$ mW, $D = 1$ mm	$\Omega_0^{ \frac{1}{2}, \frac{1}{2}\rangle \rightarrow \frac{3}{2}, \frac{3}{2}\rangle}$	$2\pi \times 20.0(16)$ MHz	

Table 14: ${}^3P_2 \rightarrow {}^3S_1$ transition (red repumper for green clock).

Parameter	Symbol	Value	Ref.
Frequency	ω_0	$2\pi \times 389.259\,833\,7(6)$ THz	[190]
Transition Energy	$\hbar\omega_0$	1.609 849 319 9(24) eV	
Wavelength (vacuum)	λ	770.160 284(11) nm	
Wavelength (air)	λ_{air}	769.955 919(8) nm	
Wavenumber (vacuum)	$k_L/2\pi$	12 984.310 422(19) cm^{-1}	
Lifetime excited state	τ	13.8(17) ns R_B : 1.4	[135, 196]
Decay rate	Γ	$7.2(9) \times 10^7 \text{ s}^{-1}$	
Natural Line Width	$\Delta\nu_{\text{FWHM}}$	$2\pi \times 11.5(14)$ MHz	
Branching Ratios	$\beta_{3S_1 \rightarrow 3P_2}$ $\beta_{3S_1 \rightarrow 3P_1}$ $\beta_{3S_1 \rightarrow 3P_0}$ $\beta_{3S_1 \rightarrow 1P_1}$	0.508(26) 0.360(25) 0.130(13) 0.0021(9)	[132]
Partial decay rate	Γ_{partial}	$3.7(5) \times 10^7 \text{ s}^{-1}$	
Recoil velocity	v_r	~ 3.031 mm/s	
Recoil energy	ω_r	$\sim 2\pi \times 1.968$ kHz	
Recoil temperature	T_r	~ 189 nK	
Doppler shift ($v = v_r$)	$\Delta\omega_d$	$\sim 2\pi \times 3.936$ kHz	
Doppler Temperature	T_D	277(33) μK	
Reduced E1 Matrix Element	$\langle J er J' \rangle_R$	4.99(32) ea_0	
Rabi Frequency $P = 1$ mW, $D = 1$ mm	$\Omega_0^{ \frac{5}{2}, \frac{5}{2}\rangle \rightarrow \frac{3}{2}, \frac{3}{2}\rangle}$	$2\pi \times 39.5(26)$ MHz	

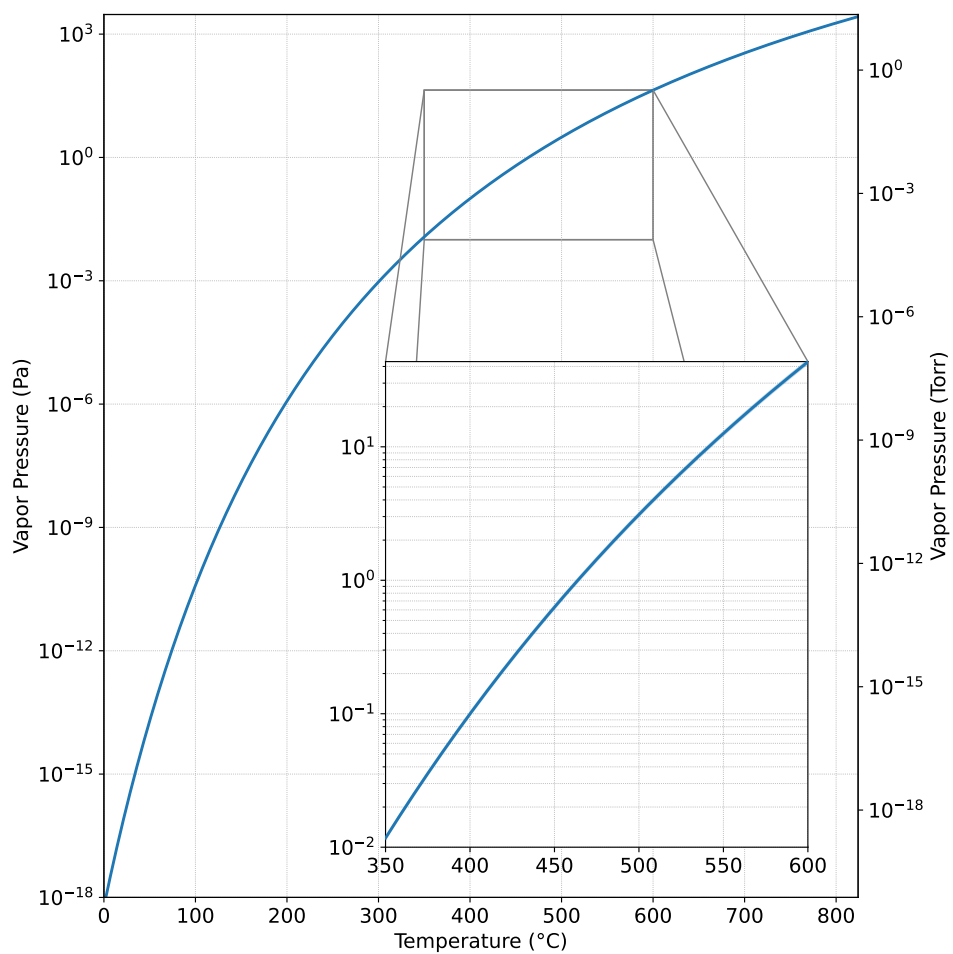


Figure 1: Vapor pressure of ytterbium as a function of temperature, calculated using Eq. (7).

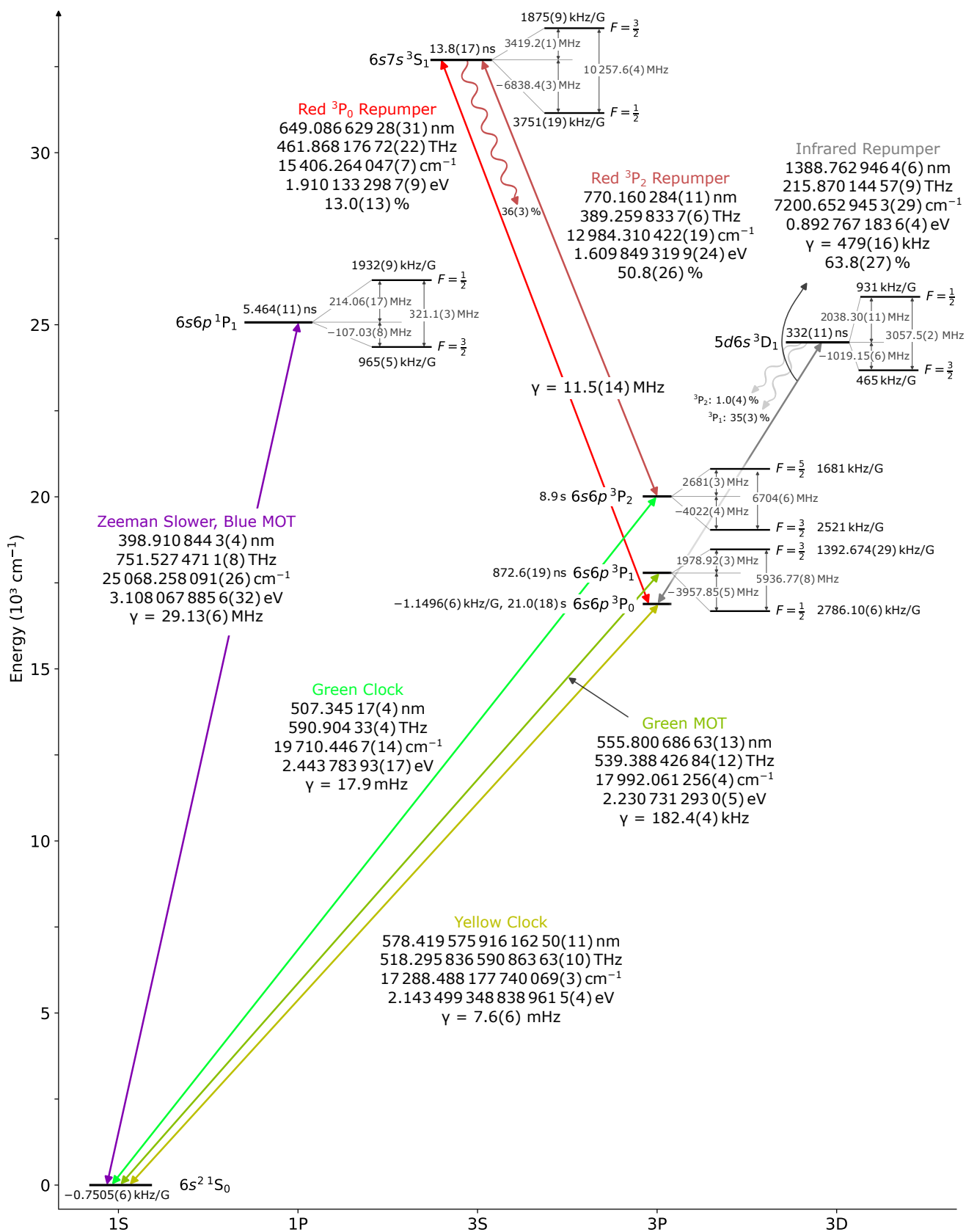


Figure 2: Data of the transitions discussed in this reference. Tables 8 to 14 list the frequencies, wavelengths, energies, linewidths, and branching ratios of the transitions as well as the lifetime of the states with the corresponding references. The Zeeman splittings between adjacent magnetic sublevels can be found in Table 5.

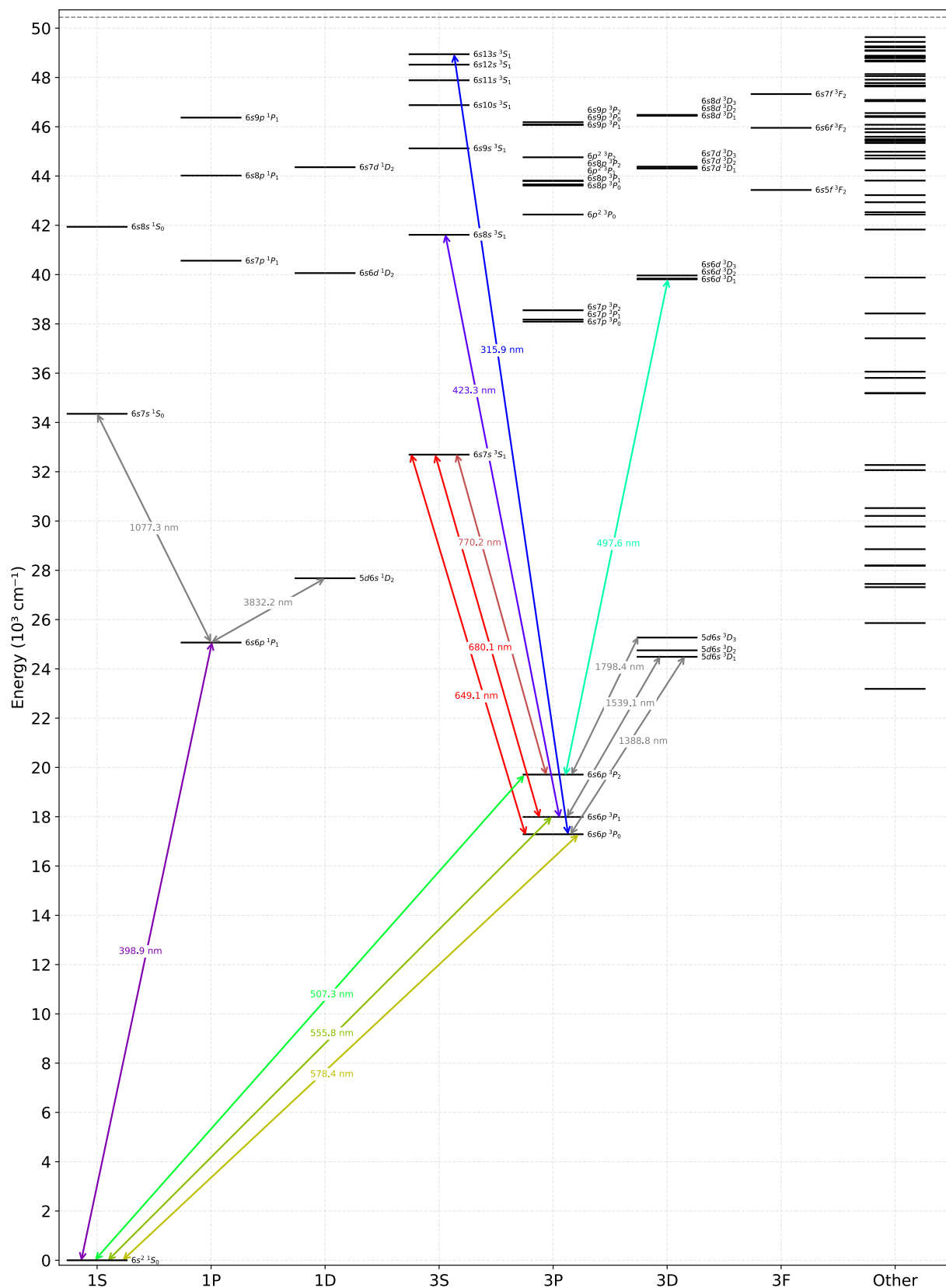


Figure 3: Neutral YbI energy level diagram with selected optical transitions. Level energies and transition wavelengths are taken from the NIST Atomic Spectra Database [60]. The dashed gray line shows the ionization energy. The ‘Other’ column summarizes all other levels that include, e.g., an inner-shell excited electron.

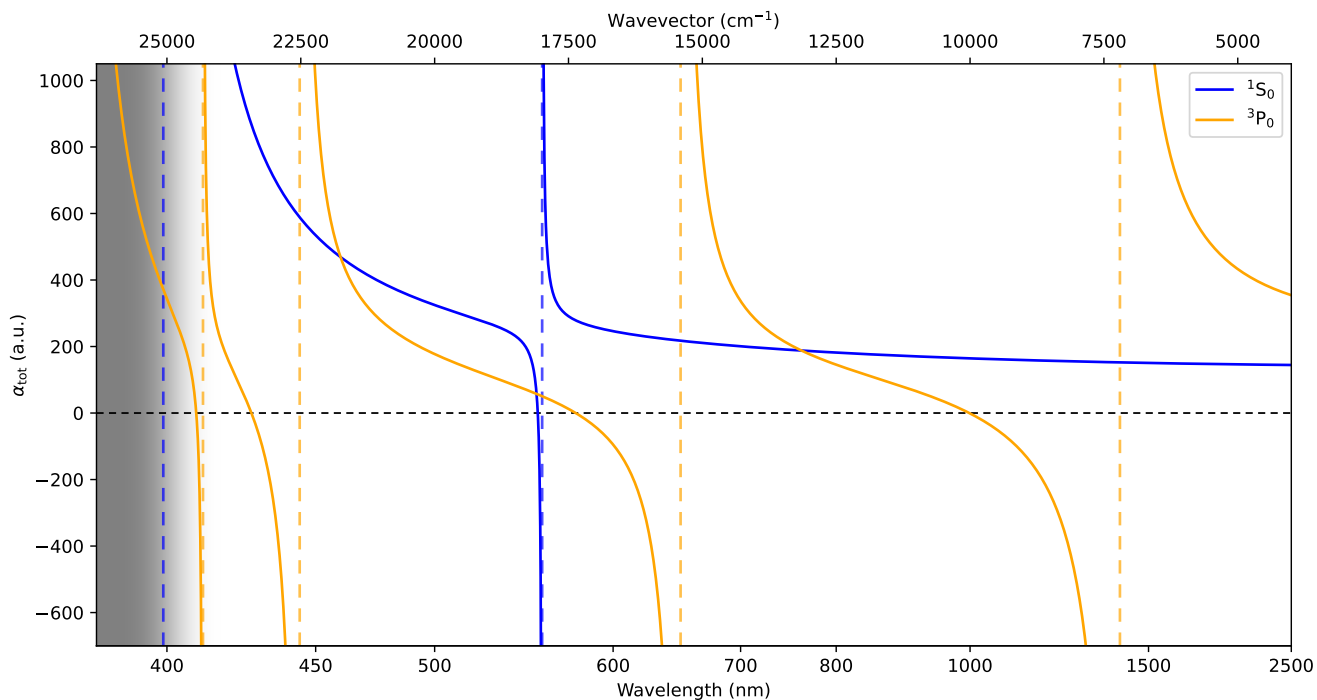


Figure 4: Polarizability of 1S_0 and 3P_0 states calculated using the semi-empirical model discussed in Refs. [156, 157]. Note the nonlinearity of the wavelength axis. At short wavelengths, as indicated by the gray shaded area, the accuracy of the semi-empirical model starts to break down.

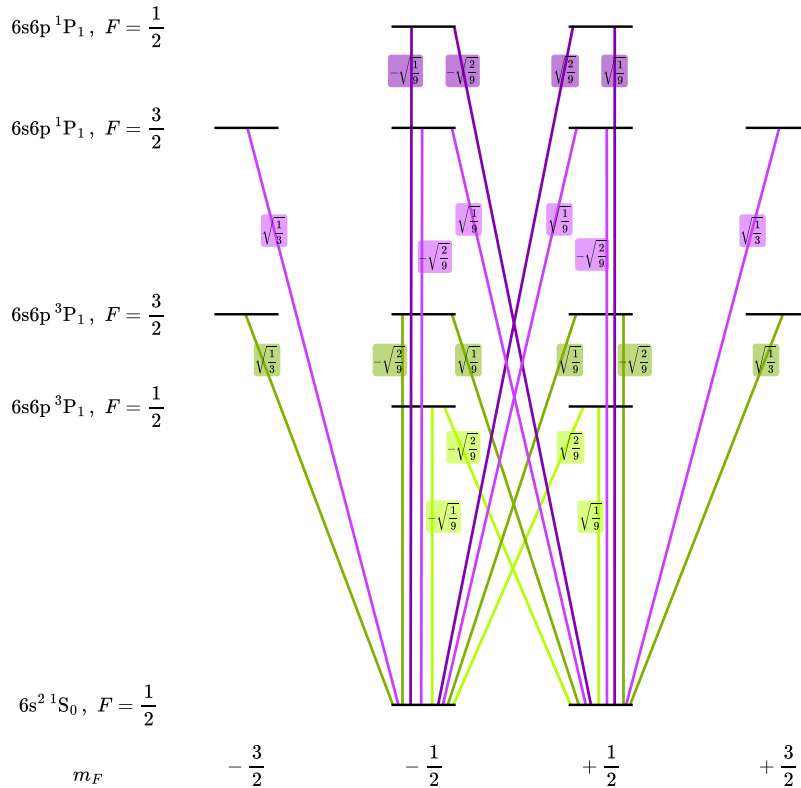


Figure 5: Dipole matrix elements for $|^1S_0, F, m_F\rangle \rightarrow |^3P_1, F', m_{F'}\rangle$ and $|^1S_0, F, m_F\rangle \rightarrow |^1P_1, F', m_{F'}\rangle$ transitions as multiples of the reduced matrix element $\langle J || e\vec{r} || J' \rangle_R$.

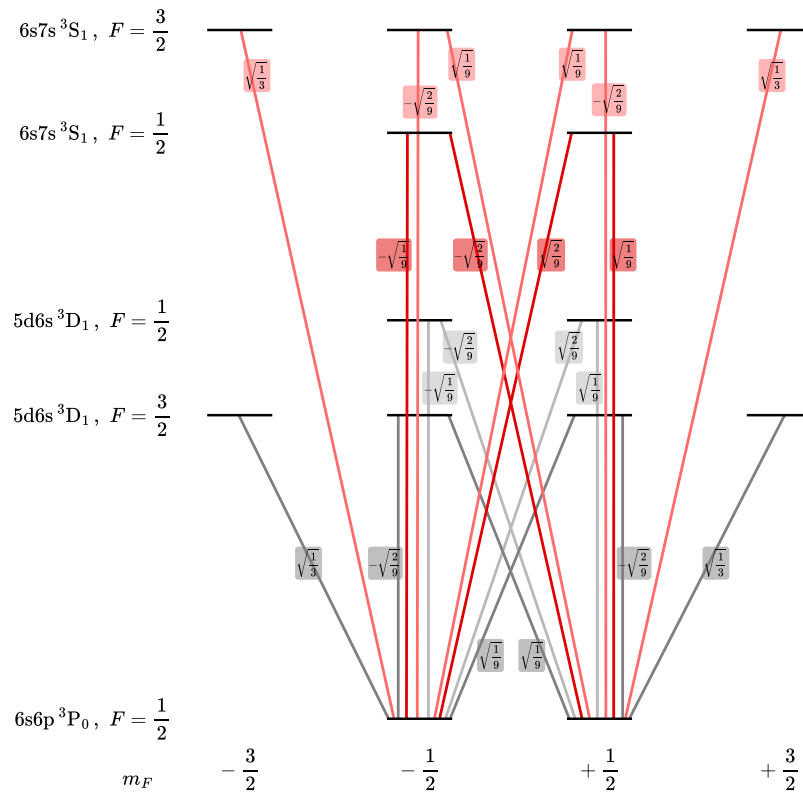


Figure 6: Dipole matrix elements for $|^3P_0, F, m_F\rangle \rightarrow |^3D_1, F', m_{F'}\rangle$ and $|^3P_0, F, m_F\rangle \rightarrow |^3S_1, F', m_{F'}\rangle$ transitions as multiples of the reduced matrix element $\langle J || e\vec{r} || J' \rangle_R$.

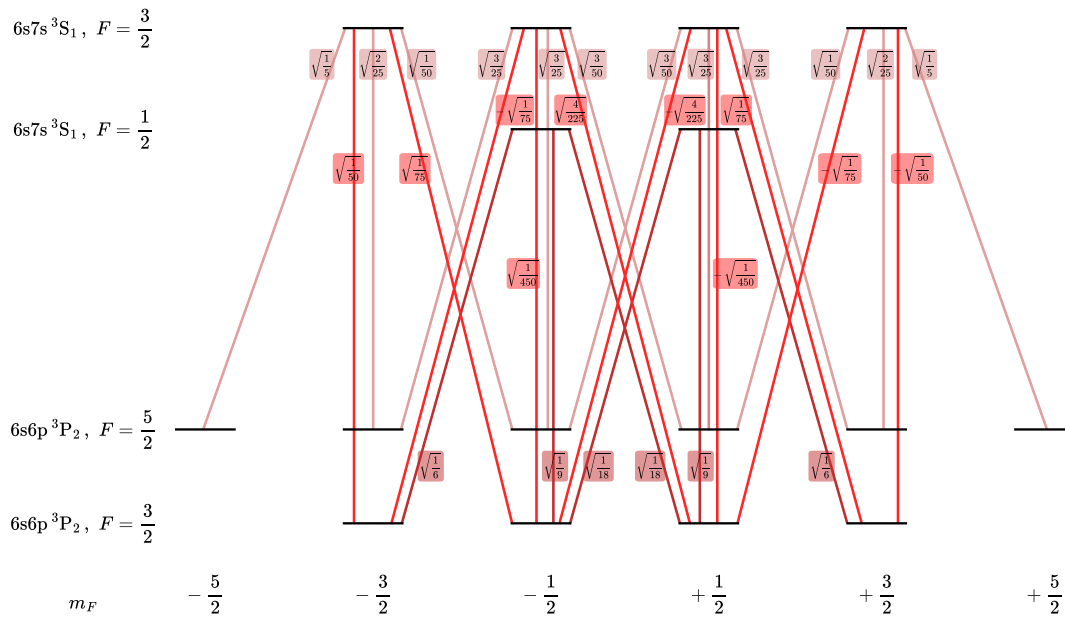


Figure 7: Dipole matrix elements for $|^3P_2, F, m_F\rangle \rightarrow |^3S_1, F', m_{F'}\rangle$ transitions as multiples of the reduced matrix element $\langle J || e\vec{r} || J' \rangle_R$.

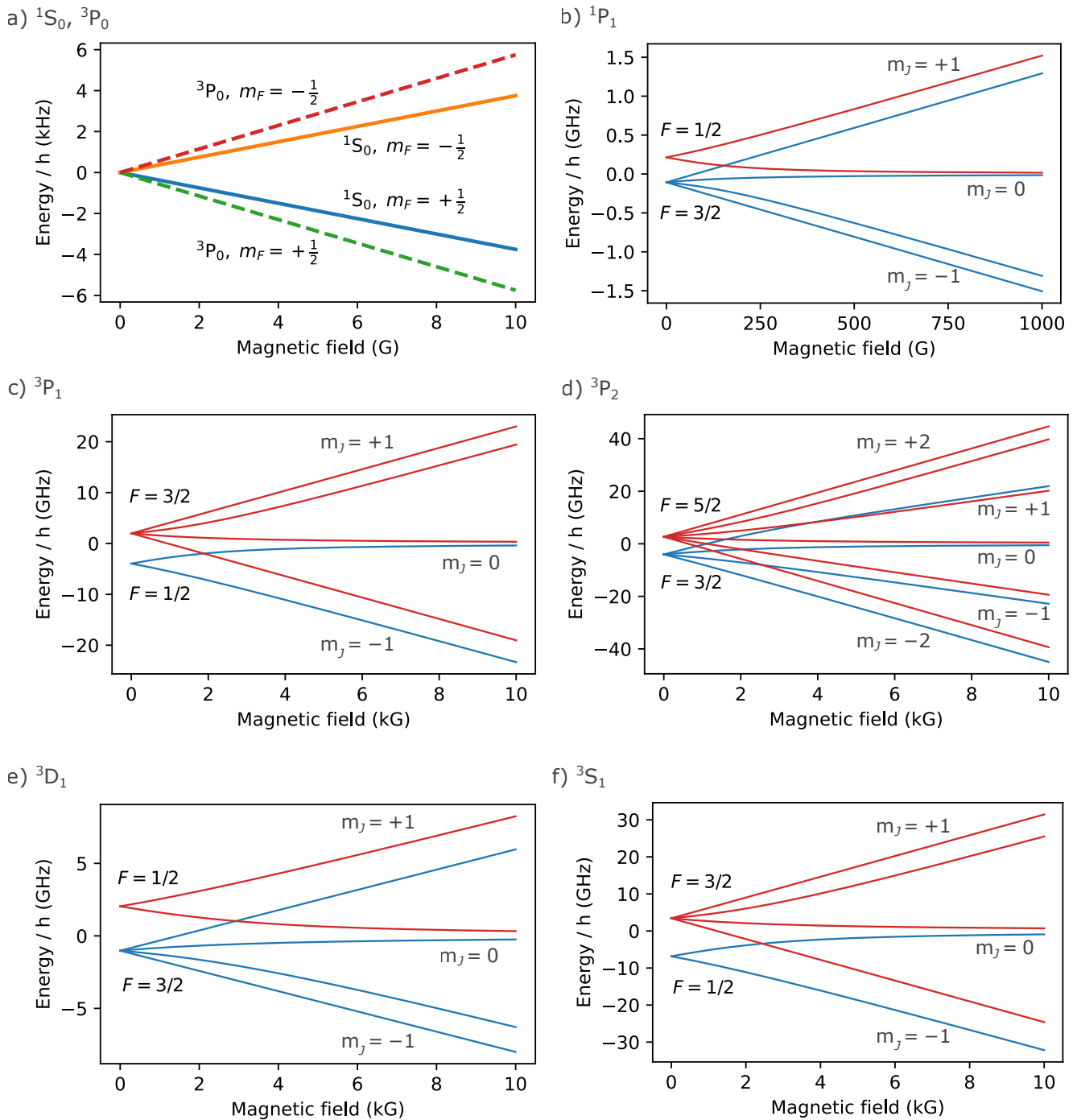


Figure 8: Eigenvalues of the combined hyperfine and Zeeman Hamiltonian, $H = H_{\text{hfs}} + H_B$, as a function of magnetic field strength. In the low-field (Zeeman) regime, each level is labeled with their respective quantum number F ; in the high-field (hyperfine Paschen-Back) regime, levels are labeled with the electronic magnetic quantum number m_J . For the 1S_0 and 3P_0 states, we use the experimental values from Table 5.

ACKNOWLEDGMENTS

We thank Monika Aidelsburger, William Cairncross, Jacob Covey, Wentao Fan, Frederic Hummel, Alessandro Muzi Falconi, Riccardo Pennetta, and Tao Zheng for stimulating discussions, comments, corrections, and suggestions. R.M.K. acknowledges support from the Alexander von Humboldt Stiftung. S.L.K. acknowledges support from the Independent Research Fund Denmark.

RELEASE NOTES

v2

- Include isotope shifts for the 3P_2 state. Accordingly update isotope shifts for the 3S_1 state, noting that this, however, yields large Birge ratios.
- Update the hyperfine structure constant for 3P_2 with one additional reference.
- Update the 759 nm magic wavelength with one additional reference.
- Add stretched-state magic-wavelength measurements obtained in ^{174}Yb to Table 7, along with supporting justification in the main text for applying them to fermionic isotopes.
- Fixed an error in Table 7 where two polarizability entries were swapped.
- Replace preprint citations with journal-published references, where available.

v1

Original release.

REFERENCES

- [1] D. A. Steck, Sodium D Line Data, Available online at <http://steck.us/alkalidata> (2024), revision 2.3.3, original revision posted 27 May 2000.
- [2] D. A. Steck, Rubidium 85 D Line Data, Available online at <http://steck.us/alkalidata> (2024), revision 2.3.3, original revision posted 30 April 2008.
- [3] D. A. Steck, Rubidium 87 D Line Data, Available online at <http://steck.us/alkalidata> (2024), revision 2.3.3, original revision posted 25 September 2001.
- [4] D. A. Steck, Cesium D Line Data, Available online at <http://steck.us/alkalidata> (2024), revision 2.3.3, original revision posted 23 January 1998.
- [5] S. Pucher, S. L. Kristensen, and R. M. Kroeze, ^{88}Sr Reference Data (2025), arXiv:2507.10487.
- [6] S. J. Masson, J. P. Covey, S. Will, and A. Asenjo-Garcia, Dicke Superradiance in Ordered Arrays of Multilevel Atoms, *PRX Quantum* **5**, 010344 (2024).
- [7] M. S. Safronova, S. G. Porsev, C. Sanner, and J. Ye, Two Clock Transitions in Neutral Yb for the Highest Sensitivity to Variations of the Fine-Structure Constant, *Phys. Rev. Lett.* **120**, 173001 (2018).
- [8] V. A. Dzuba, V. V. Flambaum, and S. Schiller, Testing physics beyond the standard model through additional clock transitions in neutral ytterbium, *Phys. Rev. A* **98**, 022501 (2018).
- [9] T. Ishiyama, K. Ono, T. Takano, A. Sunaga, and Y. Takahashi, Observation of an Inner-Shell Orbital Clock Transition in Neutral Ytterbium Atoms, *Phys. Rev. Lett.* **130**, 153402 (2023).
- [10] R. T. Birge, The Calculation of Errors by the Method of Least Squares, *Phys. Rev.* **40**, 207 (1932).
- [11] M. Trassinelli and M. Maxton, A minimalistic and general weighted averaging method for inconsistent data (2024), arXiv:2406.08293.
- [12] W. M. Haynes, *CRC Handbook of Chemistry and Physics* (CRC Press, Boca Raton, Florida, 2016).
- [13] C. Fry and M. Thoennessen, Discovery of dysprosium, holmium, erbium, thulium, and ytterbium isotopes, *Data Nucl. Data Tables* **99**, 520 (2013).
- [14] F. Kondev, M. Wang, W. Huang, S. Naimi, and G. Audi, The NUBASE2020 evaluation of nuclear physics properties, *Chin. Phys. C* **45**, 030001 (2021).
- [15] P. J. Mohr, D. B. Newell, B. N. Taylor, and E. Tiesinga, CODATA recommended values of the fundamental physical constants: 2022, *Rev. Mod. Phys.* **97**, 025002 (2025).
- [16] M. Wang, W. Huang, F. Kondev, G. Audi, and S. Naimi, The AME 2020 atomic mass evaluation (II). Tables, graphs and references, *Chin. Phys. C* **45**, 030003 (2021).
- [17] J. Wang, T. Ren, H. Lu, T. Zhou, and Y. Zhou, The absolute isotopic composition and atomic weight of ytterbium using multi-collector inductively coupled plasma mass spectrometry and development of an SI-traceable ytterbium isotopic certified reference material, *J. Anal. Spectrom.* **30**, 1377 (2015).

- [18] T. Prohaska, J. Irrgeher, J. Benefield, J. K. Böhlke, L. A. Chesson, T. B. Coplen, T. Ding, P. J. H. Dunn, M. Gröning, N. E. Holden, H. A. J. Meijer, H. Moossen, A. Possolo, Y. Takahashi, J. Vogl, T. Walczyk, J. Wang, M. E. Wieser, S. Yoneda, X.-K. Zhu, and J. Meija, Standard atomic weights of the elements 2021 (IUPAC Technical Report), *Pure Appl. Chem.* **94**, 573 (2022).
- [19] J. W. Arblaster, *Selected Values of the Crystallographic Properties of the Elements* (ASM International, Materials Park, Ohio, 2018).
- [20] C. B. Alcock, V. P. Itkin, and M. K. Horrigan, Vapour Pressure Equations for the Metallic Elements: 298-2500 K, *Can. Met. Q.* **23**, 309 (1984).
- [21] M. Kaja, D. Studer, R. Heinke, T. Kieck, and K. Wendt, Characterization of the field ionization extension for the laser ion source and trap: Measurement of the ionization potential of ytterbium, *Nucl. Instruments Methods Phys. Res. Sect. B Beam Interact. with Mater. Atoms* **547**, 165213 (2024).
- [22] H. Lehec, A. Zuliani, W. Maineult, E. Luc-Koenig, P. Pillet, P. Cheinet, F. Niyaz, and T. F. Gallagher, Laser and microwave spectroscopy of even-parity Rydberg states of neutral ytterbium and multichannel-quantum-defect-theory analysis, *Phys. Rev. A* **98**, 062506 (2018).
- [23] P. Chhetri, C. Moodley, S. Raeder, M. Block, F. Giacoppo, S. Götz, F. Heßberger, M. Eibach, O. Kaleja, M. Laatiaoui, A. Mistry, T. Murböck, and T. Walther, Investigation of the First Ionization Potential of Ytterbium in Argon Buffer Gas, *Acta Phys. Pol. B* **49**, 599 (2018).
- [24] M. Aymar, R. J. Champeau, C. Delsart, and O. Robaux, Three-step laser spectroscopy and multichannel quantum defect analysis of odd-parity Rydberg states of neutral ytterbium, *J. Phys. B Mol. Phys.* **17**, 3645 (1984).
- [25] P. Camus, A. Debarre, and C. Morillon, Highly excited levels of neutral ytterbium. I. Two-photon and two-step spectroscopy of even spectra, *J. Phys. B Mol. Phys.* **13**, 1073 (1980).
- [26] P. Camus and F. S. Tomkins, Spectre d'absorption de Yb I, *J. Phys.* **30**, 545 (1969).
- [27] G. R. Hertel, Surface Ionization. III. The First Ionization Potentials of the Lanthanides, *J. Chem. Phys.* **48**, 2053 (1968).
- [28] K. F. Zmbov and J. L. Margrave, The First Ionization Potentials of Samarium, Europium, Gadolinium, Dysprosium, Holmium, Erbium, Thulium, and Ytterbium by the Electron-Impact Method, *J. Phys. Chem.* **70**, 3014 (1966).
- [29] M. J. Dresser and D. E. Hudson, Surface Ionization of Some Rare Earths on Tungsten, *Phys. Rev.* **137**, A673 (1965).
- [30] N. Ueda, Ionization Energy Difference between Isotopes and its Effect on Isotope Abundance Measurement by Surface Ionization Method, *J. Mass Spectrom. Soc. Jpn.* **17**, 643 (1969).
- [31] E. Braaten and H. W. Hammer, Universality in few-body systems with large scattering length, *Phys. Rep.* **428**, 259 (2006).
- [32] C. Chin, R. Grimm, P. Julienne, and E. Tiesinga, Feshbach resonances in ultracold gases, *Rev. Mod. Phys.* **82**, 1225 (2010).
- [33] G. F. Gribakin and V. V. Flambaum, Calculation of the scattering length in atomic collisions using the semiclassical approximation, *Phys. Rev. A* **48**, 546 (1993).
- [34] B. J. Verhaar, E. G. M. van Kempen, and S. J. J. M. F. Kokkelmans, Predicting scattering properties of ultracold atoms: Adiabatic accumulated phase method and mass scaling, *Phys. Rev. A* **79**, 032711 (2009).
- [35] M. Borkowski, A. A. Buchachenko, R. Ciuryło, P. S. Julienne, H. Yamada, Y. Kikuchi, K. Takahashi, Y. Takasu, and Y. Takahashi, Beyond-Born-Oppenheimer effects in sub-kHz-precision photoassociation spectroscopy of ytterbium atoms, *Phys. Rev. A* **96**, 063405 (2017).
- [36] M. Kitagawa, K. Enomoto, K. Kasa, Y. Takahashi, R. Ciuryło, P. Naidon, and P. S. Julienne, Two-color photoassociation spectroscopy of ytterbium atoms and the precise determinations of s -wave scattering lengths, *Phys. Rev. A* **77**, 012719 (2008).
- [37] T. Fukuhara, S. Sugawa, and Y. Takahashi, Bose-Einstein condensation of an ytterbium isotope, *Phys. Rev. A* **76**, 051604 (2007).
- [38] T. Fukuhara, Y. Takasu, M. Kumakura, and Y. Takahashi, Degenerate Fermi Gases of Ytterbium, *Phys. Rev. Lett.* **98**, 030401 (2007).
- [39] Y. Takasu, K. Maki, K. Komori, T. Takano, K. Honda, M. Kumakura, T. Yabuzaki, and Y. Takahashi, Spin-Singlet Bose-Einstein Condensation of Two-Electron Atoms, *Phys. Rev. Lett.* **91**, 040404 (2003).
- [40] K. Enomoto, M. Kitagawa, K. Kasa, S. Tojo, and Y. Takahashi, Determination of the s -Wave Scattering Length and the C_6 van der Waals Coefficient of ^{174}Yb via Photoassociation Spectroscopy, *Phys. Rev. Lett.* **98**, 203201 (2007).
- [41] T. Fukuhara, Y. Takasu, S. Sugawa, and Y. Takahashi, Quantum Degenerate Fermi Gases of Ytterbium Atoms, *J. Low Temp. Phys.* **148**, 441 (2007).
- [42] T. Fukuhara, S. Sugawa, Y. Takasu, and Y. Takahashi, All-optical formation of quantum degenerate mixtures, *Phys. Rev. A* **79**, 021601 (2009).
- [43] S. Taie, Y. Takasu, S. Sugawa, R. Yamazaki, T. Tsujimoto, R. Murakami, and Y. Takahashi, Realization of a $SU(2) \times SU(6)$ System of Fermions in a Cold Atomic Gas, *Phys. Rev. Lett.* **105**, 190401 (2010).
- [44] S. Sugawa, Y. Takasu, K. Enomoto, and Y. Takahashi, ULTRACOLD YTTERBIUM: GENERATION, MANY-BODY PHYSICS, AND MOLECULES, in *Annu. Rev. Cold Atoms Mol.*, Vol. 1, edited by K. W. Madison, Y. Wang, A. M. Rey, and K. Bongs (WORLD SCIENTIFIC, 2013) pp. 3–51.
- [45] T. Tomita, S. Nakajima, Y. Takasu, and Y. Takahashi, Dissipative Bose-Hubbard system with intrinsic two-body loss, *Phys. Rev. A* **99**, 031601 (2019).
- [46] L. Franchi, L. F. Livi, G. Cappellini, G. Binella, M. Inguscio, J. Catani, and L. Fallani, State-dependent interactions in ultracold ^{174}Yb probed by optical clock spectroscopy, *New J. Phys.* **19**, 103037 (2017).

- [47] R. Bouganne, M. B. Aguilera, A. Dareau, E. Soave, J. Beugnon, and F. Gerbier, Clock spectroscopy of interacting bosons in deep optical lattices, *New J. Phys.* **19**, 113006 (2017).
- [48] R. Zhang, Y. Cheng, P. Zhang, and H. Zhai, Controlling the interaction of ultracold alkaline-earth atoms, *Nat. Rev. Phys.* **2**, 213 (2020).
- [49] O. Bettermann, N. Darkwah Oppong, G. Pasqualetti, L. Riegger, I. Bloch, and S. Fölling, Clock-line photoassociation of strongly bound dimers in a magic-wavelength lattice, *Phys. Rev. A* **108**, L041302 (2023).
- [50] K. Ono, J. Kobayashi, Y. Amano, K. Sato, and Y. Takahashi, Antiferromagnetic interorbital spin-exchange interaction of ^{171}Yb , *Phys. Rev. A* **99**, 032707 (2019).
- [51] Y. Takasu, Y. Fukushima, Y. Nakamura, and Y. Takahashi, Magnetoassociation of a Feshbach molecule and spin-orbit interaction between the ground and electronically excited states, *Phys. Rev. A* **96**, 023602 (2017).
- [52] F. Scazza, C. Hofrichter, M. Höfer, P. C. De Groot, I. Bloch, and S. Fölling, Observation of two-orbital spin-exchange interactions with ultracold SU(N)-symmetric fermions, *Nat. Phys.* **10**, 779 (2014).
- [53] S. Kato, S. Sugawa, K. Shibata, R. Yamamoto, and Y. Takahashi, Control of Resonant Interaction between Electronic Ground and Excited States, *Phys. Rev. Lett.* **110**, 173201 (2013).
- [54] A. Yamaguchi, S. Uetake, S. Kato, H. Ito, and Y. Takahashi, High-resolution laser spectroscopy of a Bose-Einstein condensate using the ultranarrow magnetic quadrupole transition, *New J. Phys.* **12**, 103001 (2010).
- [55] A. Khramov, A. Hansen, W. Dowd, R. J. Roy, C. Makrides, A. Petrov, S. Kotochigova, and S. Gupta, Ultracold Heteronuclear Mixture of Ground and Excited State Atoms, *Phys. Rev. Lett.* **112**, 033201 (2014).
- [56] S. Uetake, R. Murakami, J. M. Doyle, and Y. Takahashi, Spin-dependent collision of ultracold metastable atoms, *Phys. Rev. A* **86**, 032712 (2012).
- [57] A. D. Ludlow, N. D. Lemke, J. A. Sherman, C. W. Oates, G. Quémener, J. von Stecher, and A. M. Rey, Cold-collision-shift cancellation and inelastic scattering in a Yb optical lattice clock, *Phys. Rev. A* **84**, 052724 (2011).
- [58] A. Yamaguchi, S. Uetake, D. Hashimoto, J. M. Doyle, and Y. Takahashi, Inelastic Collisions in Optically Trapped Ultracold Metastable Ytterbium, *Phys. Rev. Lett.* **101**, 233002 (2008).
- [59] H. N. Russell and F. A. Saunders, New Regularities in the Spectra of the Alkaline Earths, *Astrophys. J.* **61**, 38 (1925).
- [60] A. Kramida, Yu. Ralchenko, J. Reader, and NIST ASD Team, NIST Atomic Spectra Database (ver. 5.12), [Online]. Available: <https://physics.nist.gov/asd> [2025, August 19]. National Institute of Standards and Technology, Gaithersburg, MD. (2024).
- [61] A. Jenkins, J. W. Lis, A. Senoo, W. F. McGrew, and A. M. Kaufman, Ytterbium Nuclear-Spin Qubits in an Optical Tweezer Array, *Phys. Rev. X* **12**, 21027 (2022).
- [62] S. Ma, A. P. Burgers, G. Liu, J. Wilson, B. Zhang, and J. D. Thompson, Universal Gate Operations on Nuclear Spin Qubits in an Optical Tweezer Array of ^{171}Yb Atoms, *Phys. Rev. X* **12**, 021028 (2022).
- [63] M. Peper, Y. Li, D. Y. Knapp, M. Bileska, S. Ma, G. Liu, P. Peng, B. Zhang, S. P. Horvath, A. P. Burgers, and J. D. Thompson, Spectroscopy and Modeling of ^{171}Yb Rydberg States for High-Fidelity Two-Qubit Gates, *Phys. Rev. X* **15**, 011009 (2025).
- [64] C. J. Foot, *Atomic Physics* (Oxford University Press, Oxford, United Kingdom, 2004).
- [65] D. Das, S. Barthwal, A. Banerjee, and V. Natarajan, Absolute frequency measurements in Yb with 0.08 ppb uncertainty: Isotope shifts and hyperfine structure in the 399-nm $^1\text{S}_0 \rightarrow ^1\text{P}_1$ line, *Phys. Rev. A* **72**, 032506 (2005).
- [66] M. Kleinert, M. E. Gold Dahl, and S. Bergeson, Measurement of the Yb I $^1\text{S}_0\text{-}^1\text{P}_1$ transition frequency at 399 nm using an optical frequency comb, *Phys. Rev. A* **94**, 052511 (2016).
- [67] Y. Chaiko, Isotope shifts of resonance lines in the spectrum of ytterbium, *Opt. Spectrosc.* **20**, 424 (1966).
- [68] O. Töpper, G. H. Guthöhrlein, and P. Hillerman, unpublished.
- [69] C. J. Bowers, D. Budker, S. J. Freedman, G. Gwinner, J. E. Stalnaker, and D. DeMille, Experimental investigation of the $6s^2\ ^1\text{S}_0 \rightarrow 5d6s\ ^3\text{D}_{1,2}$ forbidden transitions in atomic ytterbium, *Phys. Rev. A* **59**, 3513 (1999).
- [70] M. Saffman, Quantum computing with atomic qubits and Rydberg interactions: progress and challenges, *J. Phys. B Mol. Opt. Phys.* **49**, 202001 (2016).
- [71] R. Blatt, H. Schnatz, and G. Werth, Precise Determination of the $^{171}\text{Yb}^+$ Ground State Hyperfine Separation, *Zeitschrift für Phys. A Atoms Nucl.* **312**, 143 (1983).
- [72] H. A. Bethe and E. E. Salpeter, *Quantum Mechanics of One- and Two-Electron Atoms* (Springer-Verlag Berlin, Heidelberg, 1957).
- [73] N. Stone, *Table of Recommended Nuclear Magnetic Dipole Moments: Part I - Long-lived States*, Tech. Rep. (International Atomic Energy Agency, Vienna, Austria, 2019).
- [74] L. Olschewski, Messung der magnetischen Kerndipolmomente an freien ^{43}Ca -, ^{87}Sr -, ^{135}Ba -, ^{137}Ba -, ^{171}Yb - und ^{173}Yb -Atomen mit optischem Pumpen, *Zeitschrift für Phys.* **249**, 205 (1972).
- [75] L. Olschewski and E. W. Otten, Bestimmung der Kerndipolmomente von ^{171}Yb und ^{173}Yb durch optisches Pumpen, *Zeitschrift für Phys.* **200**, 224 (1967).
- [76] A. C. Gossard, V. Jaccarino, and J. H. Wernick, Ytterbium NMR: Yb^{171} Nuclear Moment and Yb Metal Knight Shift, *Phys. Rev.* **133**, A881 (1964).
- [77] G. H. Fuller, Nuclear Spins and Moments, *J. Phys. Chem. Ref. Data* **5**, 835 (1976).
- [78] P. Raghavan, Table of nuclear moments, *Data Nucl. Data Tables* **42**, 189 (1989).
- [79] N. Stone, Table of nuclear magnetic dipole and electric quadrupole moments, *Data Nucl. Data Tables* **90**, 75 (2005).
- [80] M. M. Boyd, T. Zelevinsky, A. D. Ludlow, S. Blatt, T. Zanon-Willette, S. M. Foreman, and J. Ye, Nuclear spin effects in optical lattice clocks, *Phys. Rev. A* **76**, 022510 (2007).
- [81] B. R. Judd and I. Lindgren, Theory of Zeeman Effect in the Ground Multiplets of Rare-Earth Atoms, *Phys. Rev.* **122**,

- 1802 (1961).
- [82] L. Labzowsky, I. Goidenko, and P. Pyykkö, Estimates of the bound-state QED contributions to the g -factor of valence ns electrons in alkali metal atoms, *Phys. Lett. A* **258**, 31 (1999).
- [83] A. Zhang, C. Tian, Q. Zhu, B. Wang, D. Xiong, Z. Xiong, L. He, and B. Lyu, Precise measurement of ^{171}Yb magnetic constants for $^1\text{S}_0\text{-}^3\text{P}_0$ clock transition, *Chin. Phys. B* **32**, 020601 (2023).
- [84] W. F. McGrew, X. Zhang, R. J. Fasano, S. A. Schäffer, K. Beloy, D. Nicolodi, R. C. Brown, N. Hinkley, G. Milani, M. Schioppo, T. H. Yoon, and A. D. Ludlow, Atomic clock performance enabling geodesy below the centimetre level, *Nature* **564**, 87 (2018).
- [85] D. Ai, T. Jin, T. Zhang, L. Luo, L. Liu, M. Zhou, and X. Xu, Absolute frequency measurement of the $6s6p\ ^3\text{P}_0 \rightarrow 5d6s\ ^3\text{D}_1$ transition based on ultracold ytterbium atoms, *Phys. Rev. A* **107**, 063107 (2023).
- [86] D. Ai, T. Jin, T. Zhang, L. Luo, L. Liu, M. Zhou, and X. Xu, Erratum: Absolute frequency measurement of the $6s6p\ ^3\text{P}_0 \rightarrow 5d6s\ ^3\text{D}_1$ transition based on ultracold ytterbium atoms [*Phys. Rev. A* 107, 063107 (2023)], *Phys. Rev. A* **109**, 039902 (2024).
- [87] K. Ono, Y. Saito, T. Ishiyama, T. Higomoto, T. Takano, Y. Takasu, Y. Yamamoto, M. Tanaka, and Y. Takahashi, Observation of Nonlinearity of Generalized King Plot in the Search for New Boson, *Phys. Rev. X* **12**, 021033 (2022).
- [88] L. Luo, H. Qiao, D. Ai, M. Zhou, S. Zhang, S. Zhang, C. Sun, Q. Qi, C. Peng, T. Jin, W. Fang, Z. Yang, T. Li, K. Liang, and X. Xu, Absolute frequency measurement of an Yb optical clock at the 10^{-16} level using International Atomic Time, *Metrologia* **57**, 065017 (2020).
- [89] L. Riegger, *Interorbital spin exchange in a state-dependent optical lattice*, Ph.D. thesis, Ludwig-Maximilians-Universität München (2019).
- [90] Q. Gao, M. Zhou, C. Han, S. Li, S. Zhang, Y. Yao, B. Li, H. Qiao, D. Ai, G. Lou, M. Zhang, Y. Jiang, Z. Bi, L. Ma, and X. Xu, Systematic evaluation of a ^{171}Yb optical clock by synchronous comparison between two lattice systems, *Sci. Rep.* **8**, 8022 (2018).
- [91] N. Lemke, A. Ludlow, Z. Barber, T. Fortier, S. Diddams, Y. Jiang, S. Jefferts, T. Heavner, T. Parker, and C. Oates, Spin-1/2 Optical Lattice Clock, *Phys. Rev. Lett.* **103**, 063001 (2009).
- [92] N. Poli, Z. W. Barber, N. D. Lemke, C. W. Oates, L. S. Ma, J. E. Stalnaker, T. M. Fortier, S. A. Diddams, L. Hollberg, J. C. Bergquist, A. Bruschi, S. Jefferts, T. Heavner, and T. Parker, Frequency evaluation of the doubly forbidden $^1\text{S}_0\text{-}^3\text{P}_0$ transition in bosonic ^{174}Yb , *Phys. Rev. A* **77**, 050501 (2008).
- [93] Z. Barber, C. Hoyt, C. Oates, L. Hollberg, A. Taichenachev, and V. Yudin, Direct Excitation of the Forbidden Clock Transition in Neutral ^{174}Yb Atoms Confined to an Optical Lattice, *Phys. Rev. Lett.* **96**, 083002 (2006).
- [94] T. Bothwell, B. D. Hunt, J. L. Siegel, Y. S. Hassan, T. Grogan, T. Kobayashi, K. Gibble, S. G. Porsev, M. S. Safronova, R. C. Brown, K. Beloy, and A. D. Ludlow, Lattice Light Shift Evaluations in a Dual-Ensemble Yb Optical Lattice Clock, *Phys. Rev. Lett.* **134**, 033201 (2025).
- [95] G. Breit and L. A. Wills, Hyperfine Structure in Intermediate Coupling, *Phys. Rev.* **44**, 470 (1933).
- [96] A. Lurio, M. Mandel, and R. Novick, Second-Order Hyperfine and Zeeman Corrections for an (sl) Configuration, *Phys. Rev.* **126**, 1758 (1962).
- [97] A. Taichenachev, V. Yudin, C. Oates, C. Hoyt, Z. Barber, and L. Hollberg, Magnetic Field-Induced Spectroscopy of Forbidden Optical Transitions with Application to Lattice-Based Optical Atomic Clocks, *Phys. Rev. Lett.* **96**, 083001 (2006).
- [98] L. Nenadović and J. J. McFerran, Clock and inter-combination line frequency separation in ^{171}Yb , *J. Phys. B Mol. Opt. Phys.* **49**, 065004 (2016).
- [99] B. Edlén, The Refractive Index of Air, *Metrologia* **2**, 71 (1966).
- [100] E. R. Peck and K. Reeder, Dispersion of Air, *J. Opt. Soc. Am.* **62**, 958 (1972).
- [101] A. L. Buck, New Equations for Computing Vapor Pressure and Enhancement Factor, *J. Appl. Meteorol.* **20**, 1527 (1981).
- [102] Buck Research Instruments, LLC, *CR-1A Hygrometer with Autofill: Operating Manual*, Buck Research Instruments, LLC, Boulder, CO, USA (2012).
- [103] K. Enomoto, N. Hizawa, T. Suzuki, K. Kobayashi, and Y. Moriwaki, Comparison of resonance frequencies of major atomic lines in 398-423 nm, *Appl. Phys. B* **122**, 126 (2016).
- [104] T. Lauprêtre, L. Groult, B. Achi, M. Petersen, Y. Kersalé, M. Delehayé, and C. Lacroûte, Absolute frequency measurements of the $^1\text{S}_0 \rightarrow ^1\text{P}_1$ transition in ytterbium, *OSA Contin.* **3**, 50 (2020).
- [105] T. Tanabe, D. Akamatsu, H. Inaba, S. Okubo, T. Kobayashi, M. Yasuda, K. Hosaka, and F.-L. Hong, A frequency-stabilized light source at 399 nm using an Yb hollow-cathode lamp, *Jpn. J. Appl. Phys.* **57**, 062501 (2018).
- [106] A. H. Nizamani, J. J. McLoughlin, and W. K. Hensinger, Doppler-free Yb spectroscopy with the fluorescence spot technique, *Phys. Rev. A* **82**, 043408 (2010).
- [107] T. Kobayashi, A. Nishiyama, K. Hosaka, D. Akamatsu, A. Kawasaki, M. Wada, H. Inaba, T. Tanabe, and M. Yasuda, Improved absolute frequency measurement of ^{171}Yb at NMIJ with uncertainty below 2×10^{-16} , *Metrologia* **62**, 025006 (2025).
- [108] I. Goti, S. Condio, C. Clivati, M. Risaro, M. Gozzelino, G. A. Costanzo, F. Levi, D. Calonico, and M. Pizzocaro, Absolute frequency measurement of a Yb optical clock at the limit of the Cs fountain, *Metrologia* **60**, 10.1088/1681-7575/acbc5 (2023).
- [109] T. Kobayashi, A. Takamizawa, D. Akamatsu, A. Kawasaki, A. Nishiyama, K. Hosaka, Y. Hisai, M. Wada, H. Inaba, T. Tanabe, and M. Yasuda, Search for Ultralight Dark Matter from Long-Term Frequency Comparisons of Optical and Microwave Atomic Clocks, *Phys. Rev. Lett.* **129**, 241301 (2022).

- [110] C. Clivati, M. Pizzocaro, E. Bertacco, S. Condio, G. Costanzo, S. Donadello, I. Goti, M. Gozzelino, F. Levi, A. Mura, M. Risaro, D. Calonico, M. Tønnes, B. Pointard, M. Mazouth-Lauriol, R. Le Targat, M. Abgrall, M. Lours, H. Le Goff, L. Lorini, P.-E. Pottie, E. Cantin, O. Lopez, C. Chardonnet, and A. Amy-Klein, Coherent Optical-Fiber Link Across Italy and France, *Phys. Rev. Appl.* **18**, 054009 (2022).
- [111] H. Kim, M. S. Heo, C. Y. Park, D. H. Yu, and W. K. Lee, Absolute frequency measurement of the ^{171}Yb optical lattice clock at KRISS using TAI for over a year, *Metrologia* **58**, 10.1088/1681-7575/ac1950 (2021).
- [112] M. Pizzocaro, F. Bregolin, P. Barbieri, B. Rauf, F. Levi, and D. Calonico, Absolute frequency measurement of the $^1\text{S}_0$ - $^3\text{P}_0$ transition of ^{171}Yb with a link to international atomic time, *Metrologia* **57**, 10.1088/1681-7575/ab50e8 (2020).
- [113] T. Kobayashi, D. Akamatsu, K. Hosaka, Y. Hisai, M. Wada, H. Inaba, T. Suzuyama, F.-L. Hong, and M. Yasuda, Demonstration of the nearly continuous operation of an ^{171}Yb optical lattice clock for half a year, *Metrologia* **57**, 065021 (2020).
- [114] W. F. McGrew, X. Zhang, H. Leopardi, R. J. Fasano, D. Nicolodi, K. Beloy, J. Yao, J. A. Sherman, S. A. Schäffer, J. Savory, R. C. Brown, S. Römisch, C. W. Oates, T. E. Parker, T. M. Fortier, and A. D. Ludlow, Towards the optical second: verifying optical clocks at the SI limit, *Optica* **6**, 448 (2019).
- [115] H. Kim, M.-S. Heo, W.-K. Lee, C. Y. Park, H.-G. Hong, S.-W. Hwang, and D.-H. Yu, Improved absolute frequency measurement of the ^{171}Yb optical lattice clock at KRISS relative to the SI second, *Jpn. J. Appl. Phys.* **56**, 050302 (2017).
- [116] M. Pizzocaro, P. Thoumany, B. Rauf, F. Bregolin, G. Milani, C. Clivati, G. A. Costanzo, F. Levi, and D. Calonico, Absolute frequency measurement of the $^1\text{S}_0$ - $^3\text{P}_0$ transition of ^{171}Yb , *Metrologia* **54**, 102 (2017).
- [117] C. Y. Park, D.-H. Yu, W.-K. Lee, S. E. Park, E. B. Kim, S. K. Lee, J. W. Cho, T. H. Yoon, J. Mun, S. J. Park, T. Y. Kwon, and S.-B. Lee, Absolute frequency measurement of $^1\text{S}_0(F=1/2)$ - $^3\text{P}_0(F=1/2)$ transition of ^{171}Yb atoms in a one-dimensional optical lattice at KRISS, *Metrologia* **50**, 119 (2013).
- [118] M. Yasuda, H. Inaba, T. Kohno, T. Tanabe, Y. Nakajima, K. Hosaka, D. Akamatsu, A. Onae, T. Suzuyama, M. Amemiya, and F.-L. Hong, Improved Absolute Frequency Measurement of the ^{171}Yb Optical Lattice Clock towards a Candidate for the Redefinition of the Second, *Appl. Phys. Express* **5**, 102401 (2012).
- [119] T. Kohno, M. Yasuda, K. Hosaka, H. Inaba, Y. Nakajima, and F.-L. Hong, One-Dimensional Optical Lattice Clock with a Fermionic ^{171}Yb Isotope, *Appl. Phys. Express* **2**, 072501 (2009).
- [120] C. Hoyt, Z. Barber, C. Oates, T. Fortier, S. Diddams, and L. Hollberg, Observation and Absolute Frequency Measurements of the $^1\text{S}_0$ - $^3\text{P}_0$ Optical Clock Transition in Neutral Ytterbium, *Phys. Rev. Lett.* **95**, 083003 (2005).
- [121] H. S. Margolis, G. Panfilo, G. Petit, C. Oates, T. Ido, and S. Bize, The CIPM list 'Recommended values of standard frequencies': 2021 update, *Metrologia* **61**, 035005 (2024).
- [122] Consultative Committee for Time and Frequency (CCTF), Recommendation PSFS-2 (2021), 22nd meeting (session II – online).
- [123] A. Yamaguchi, *Metastable State of Ultracold and Quantum Degenerate Ytterbium Atoms: High-Resolution Spectroscopy and Cold Collisions*, Ph.D. thesis, Kyoto University (2008).
- [124] C. Frugiuele, E. Fuchs, G. Perez, and M. Schlafler, Constraining new physics models with isotope shift spectroscopy, *Phys. Rev. D* **96**, 015011 (2017).
- [125] J. C. Berengut, D. Budker, C. Delaunay, V. V. Flambaum, C. Frugiuele, E. Fuchs, C. Grojean, R. Harnik, R. Ozeri, G. Perez, and Y. Soreq, Probing New Long-Range Interactions by Isotope Shift Spectroscopy, *Phys. Rev. Lett.* **120**, 091801 (2018).
- [126] N. L. Figueroa, J. C. Berengut, V. A. Dzuba, V. V. Flambaum, D. Budker, and D. Antypas, Precision Determination of Isotope Shifts in Ytterbium and Implications for New Physics, *Phys. Rev. Lett.* **128**, 073001 (2022).
- [127] W. A. van Wijngaarden and J. Li, Measurement of isotope shifts and hyperfine splittings of ytterbium by means of acousto-optic modulation, *J. Opt. Soc. Am. B* **11**, 2163 (1994).
- [128] D. L. Clark, M. E. Cage, D. A. Lewis, and G. W. Greenlees, Optical isotopic shifts and hyperfine splittings for Yb, *Phys. Rev. A* **20**, 239 (1979).
- [129] A. P. Mishra and T. Balasubramanian, Radiative lifetimes of the first excited $^3\text{P}_{2,0}^o$ metastable levels in Kr I, Xe I, Yb I and Hg-like atoms, *J. Quant. Spectrosc. Radiat. Transf.* **69**, 769 (2001).
- [130] S. G. Porsev and A. Derevianko, Hyperfine quenching of the metastable $^3\text{P}_{0,2}$ states in divalent atoms, *Phys. Rev. A* **69**, 042506 (2004).
- [131] K. Honda, Y. Takahashi, T. Kuwamoto, M. Fujimoto, K. Toyoda, K. Ishikawa, and T. Yabuzaki, Magneto-optical trapping of Yb atoms and a limit on the branching ratio of the $^1\text{P}_1$ state, *Phys. Rev. A* **59**, R934 (1999).
- [132] S. G. Porsev, Y. G. Rakhlina, and M. G. Kozlov, Electric-dipole amplitudes, lifetimes, and polarizabilities of the low-lying levels of atomic ytterbium, *Phys. Rev. A* **60**, 2781 (1999).
- [133] K. B. Blagoev, V. A. Komarovskii, and N. P. Penkin, *Opt. Spectrosc.* **45**, 832 (1978).
- [134] M. L. Burshtein, Y. F. Verolainen, V. A. Komarovskii, A. L. Osherovich, and N. P. Penkin, Lifetimes of the $^3\text{P}_1$ level of Yb I and the $^2\text{P}_{3/2,1/2}$ level of Yb II, *Opt. Spectrosc.* **37**, 351 (1974).
- [135] W. Lange, J. Luther, and A. Stendel, in *Proceedings, 2nd Conference of European Group for Atomic Spectroscopy* (Hanover, 1970) p. 31.
- [136] V. A. Komarovskii and N. P. Penkin, Oscillator Strengths of the Spectral Lines of Tm I and Yb I, *Opt. Spectrosc.* **26**, 483 (1969).
- [137] C. J. Bowers, D. Budker, E. D. Commins, D. DeMille, S. J. Freedman, A.-T. Nguyen, S.-Q. Shang, and M. Zolotarev, Experimental investigation of excited-state lifetimes in atomic ytterbium, *Phys. Rev. A* **53**, 3103 (1996).
- [138] K. Blagoev and V. Komarovskii, Lifetimes of Levels of Neutral and Singly Ionized Lanthanide Atoms, *Data Nucl. Data*

- Tables **56**, 1 (1994).
- [139] F. H. K. Rambow and L. D. Schearer, Radiative lifetimes and alignment depolarization cross sections for YbI and II by the Hanle effect in a flowing helium system, *Phys. Rev. A* **14**, 738 (1976).
- [140] A. Corney, *Atomic and Laser Spectroscopy* (Clarendon Press, Oxford University Press, Oxford, United Kingdom, 1977).
- [141] W. Demtröder, *Laser Spectroscopy* (Springer-Verlag Berlin, Heidelberg, Germany, 2008).
- [142] D. M. Brink and G. R. Satchler, *Angular Momentum*, Oxford Library of the Physical Sciences (Clarendon Press, Oxford, 1968).
- [143] D. A. Steck, Quantum and Atom Optics, Available online at <http://steck.us/teaching> (2007), revision 0.16.4, 7 May 2025.
- [144] P. Barakhshan, A. Marrs, A. Bhosale, B. Arora, R. Eigenmann, and M. S. Safronova, Portal for High-Precision Atomic Data and Computation (version 2.0), University of Delaware, Newark, DE, USA. <https://www.udel.edu/atom> (2022), accessed May 25, 2025. Original data source cited where available.
- [145] P. D. Lett, R. N. Watts, C. I. Westbrook, W. D. Phillips, P. L. Gould, and H. J. Metcalf, Observation of Atoms Laser Cooled below the Doppler Limit, *Phys. Rev. Lett.* **61**, 169 (1988).
- [146] C. Y. Park and T. H. Yoon, Efficient magneto-optical trapping of Yb atoms with a violet laser diode, *Phys. Rev. A* **68**, 055401 (2003).
- [147] T. Kuwamoto, K. Honda, Y. Takahashi, and T. Yabuzaki, Magneto-optical trapping of Yb atoms using an intercombination transition, *Phys. Rev. A* **60**, R745 (1999).
- [148] S. Dörscher, A. Thobe, B. Hundt, A. Kochanek, R. Le Targat, P. Windpassinger, C. Becker, and K. Sengstock, Creation of quantum-degenerate gases of ytterbium in a compact 2D-/3D-magneto-optical trap setup, *Rev. Sci. Instrum.* **84**, 10.1063/1.4802682 (2013).
- [149] A. Guttridge, S. A. Hopkins, S. L. Kemp, D. Boddy, R. Freytag, M. P. A. Jones, M. R. Tarbutt, E. A. Hinds, and S. L. Cornish, Direct loading of a large Yb MOT on the $^1S_0 \rightarrow ^3P_1$ transition, *J. Phys. B Mol. Opt. Phys.* **49**, 145006 (2016).
- [150] J. Lee, J. H. Lee, J. Noh, and J. Mun, Core-shell magneto-optical trap for alkaline-earth-metal-like atoms, *Phys. Rev. A* **91**, 053405 (2015).
- [151] H. Letellier, Á. Mitchell Galvão de Melo, A. Dorne, and R. Kaiser, Loading of a large Yb MOT on the $^1S_0 \rightarrow ^1P_1$ transition, *Rev. Sci. Instrum.* **94**, 0 (2023).
- [152] R. Grimm, M. Weidemüller, and Y. B. Ovchinnikov, Optical Dipole Traps for Neutral Atoms, in *Advances in Atomic, Molecular, and Optical Physics*, Vol. 42 (Academic Press, 2000) pp. 95–170.
- [153] F. Le Kien, P. Schneeweiss, and A. Rauschenbeutel, Dynamical polarizability of atoms in arbitrary light fields: general theory and application to cesium, *Eur. Phys. J. D* **67**, 92 (2013).
- [154] V. V. Tsyganok, D. A. Pershin, E. T. Davletov, V. A. Khlebnikov, and A. V. Akimov, Scalar, tensor, and vector polarizability of Tm atoms in a 532-nm dipole trap, *Phys. Rev. A* **100**, 042502 (2019).
- [155] A. T. Muzi Falconi, *Trapping, loading and imaging fermionic ytterbium atom arrays*, Ph.D. thesis, University of Trieste (2025).
- [156] T. O. Höhn, E. Staub, G. Brochier, N. Darkwah Oppong, and M. Aidelsburger, State-dependent potentials for the 1S_0 and 3P_0 clock states of neutral ytterbium atoms, *Phys. Rev. A* **108**, 053325 (2023).
- [157] T. O. Höhn, *State-dependent potentials and clock ground-state cooling in an ytterbium quantum simulator*, Ph.D. thesis, Ludwig-Maximilians-Universität München (2024).
- [158] Z.-M. Tang, Y.-M. Yu, J. Jiang, and C.-Z. Dong, Magic wavelengths for the $6s^2 \ ^1S_0$ - $6s6p \ ^3P_1^o$ transition in ytterbium atom, *J. Phys. B Mol. Opt. Phys.* **51**, 125002 (2018).
- [159] V. A. Dzuba and A. Derevianko, Dynamic polarizabilities and related properties of clock states of the ytterbium atom, *J. Phys. B Mol. Opt. Phys.* **43**, 074011 (2010).
- [160] S. Sashkin, J. T. Wilson, B. Grinkemeyer, and J. D. Thompson, Narrow-Line Cooling and Imaging of Ytterbium Atoms in an Optical Tweezer Array, *Phys. Rev. Lett.* **122**, 143002 (2019).
- [161] R. Yamamoto, J. Kobayashi, T. Kuno, K. Kato, and Y. Takahashi, An ytterbium quantum gas microscope with narrow-line laser cooling, *New J. Phys.* **18**, 023016 (2016).
- [162] T. O. Höhn, R. A. Villela, E. Zu, L. Bezzo, R. M. Kroeze, and M. Aidelsburger, Determining the 3P_0 Excited-State Tune-Out Wavelength of ^{174}Yb in a Triple-Magic Lattice, *PRX Quantum* **7**, 010303 (2026).
- [163] T. Ishiyama, K. Ono, R. Asano, H. Kawase, T. Takano, A. Sunaga, Y. Yamamoto, M. Tanaka, and Y. Takahashi, Excluding Hypothetical Light Boson Interpretation of Yb King Plot Nonlinearity with the $^1S_0 \leftrightarrow ^3P_2$ Isotope Shift Measurement (2026), arXiv:2601.08487.
- [164] A. Aeppli, W. J. Arthur-Dworschack, K. Beloy, C. M. Berry, T. Bothwell, A. Folz, T. M. Fortier, T. Grogan, Y. S. Hassan, Z. Z. Hu, D. B. Hume, B. D. Hunt, K. Kim, A. Koepke, D. Lee, D. R. Leibbrandt, B. Lewis, A. D. Ludlow, M. C. Marshall, N. V. Nardelli, H. Ranganath, D. A. R. Castillo, J. A. Sherman, J. L. Siegel, S. Thornton, W. Warfield, and J. Ye, Atomic clock frequency ratios with fractional uncertainty $\leq 3.2 \times 10^{-18}$ (2025), arXiv:2512.21428.
- [165] N. Nemitz, A. A. Jørgensen, R. Yanagimoto, F. Bregolin, and H. Katori, Modeling light shifts in optical lattice clocks, *Phys. Rev. A* **99**, 033424 (2019).
- [166] T. Kobayashi, D. Akamatsu, Y. Hisai, T. Tanabe, H. Inaba, T. Suzuyama, F.-L. Hong, K. Hosaka, and M. Yasuda, Uncertainty Evaluation of an ^{171}Yb Optical Lattice Clock at NMIJ, *IEEE Trans. Ultrason. Ferroelectr. Freq. Control* **65**, 2449 (2018).
- [167] R. C. Brown, N. B. Phillips, K. Beloy, W. F. McGrew, M. Schioppo, R. J. Fasano, G. Milani, X. Zhang, N. Hinkley, H. Leopardi, T. H. Yoon, D. Nicolodi, T. M. Fortier, and A. D. Ludlow, Hyperpolarizability and Operational Magic

- Wavelength in an Optical Lattice Clock, Phys. Rev. Lett. **119**, 253001 (2017).
- [168] N. Nemitz, T. Ohkubo, M. Takamoto, I. Ushijima, M. Das, N. Ohmae, and H. Katori, Frequency ratio of Yb and Sr clocks with 5×10^{-17} uncertainty at 150 seconds averaging time, Nat. Photonics **10**, 258 (2016).
- [169] Y. Li, Y. Bao, M. Peper, C. Li, and J. D. Thompson, Fast, continuous and coherent atom replacement in a neutral atom qubit array (2025), arXiv:2506.15633.
- [170] I. Angeli and K. P. Marinova, Table of experimental nuclear ground state charge radii: An update, Data Nucl. Data Tables **99**, 69 (2013).
- [171] M. Baumann and G. Wandel, g_J Factors of the $6s6p\ ^3P_1$ and $6s6p\ ^1P_1$ states of ytterbium, Phys. Lett. A **28**, 200 (1968).
- [172] W.-L. Wang and X.-Y. Xu, A novel method to measure the isotope shifts and hyperfine splittings of all ytterbium isotopes for a 399-nm transition, Chin. Phys. B **19**, 123202 (2010).
- [173] A. Banerjee, U. D. Rapol, D. Das, A. Krishna, and V. Natarajan, Precise measurements of UV atomic lines: Hyperfine structure and isotope shifts in the 398.8 nm line of Yb, Eur. Lett. **63**, 340 (2003).
- [174] R. Zinkstok, E. J. van Duijn, S. Witte, and W. Hogervorst, Hyperfine structure and isotope shift of transitions in Yb I using UV and deep-UV cw laser light and the angular distribution of fluorescence radiation, J. Phys. B Mol. Opt. Phys. **35**, 305 (2002).
- [175] T. Loftus, J. R. Bochinski, and T. W. Mossberg, Optical double-resonance cooled-atom spectroscopy, Phys. Rev. A **63**, 023402 (2001).
- [176] K. Deilamian, J. D. Gillaspay, and D. E. Kelleher, Isotope shifts and hyperfine splittings of the 398.8-nm Yb I line, J. Opt. Soc. Am. B **10**, 789 (1993).
- [177] R. W. Berends and L. Maleki, Hyperfine structure and isotope shifts of transitions in neutral and singly ionized ytterbium, J. Opt. Soc. Am. B **9**, 332 (1992).
- [178] H. Liening, Level-crossing-spectroscopy with additional optical pumping in the ground state, Zeitschrift für Phys. A Atoms Nucl. **320**, 363 (1985).
- [179] P. Grundevik, M. Gustavsson, A. Rosén, and S. Rydberg, Analysis of the isotope shifts and hyperfine structure in the $3\ 988\ \text{\AA}$ ($6s6p\ ^1P_1 \leftrightarrow 6s^2\ ^1S_0$) YbI line, Zeitschrift für Phys. A Atoms Nucl. **292**, 307 (1979).
- [180] B. Budick and J. Snir, g_J values of excited states of the ytterbium atom, Phys. Lett. A **24**, 689 (1967).
- [181] D. M. Jones, F. van Kann, and J. J. McFerran, Intercombination line frequencies in ^{171}Yb validated with the clock transition, Appl. Opt. **62**, 3932 (2023).
- [182] P. E. Atkinson, J. S. Schelfhout, and J. J. McFerran, Hyperfine constants and line separations for the 1S_0 - 3P_1 intercombination line in neutral ytterbium with sub-Doppler resolution, Phys. Rev. A **100**, 042505 (2019).
- [183] J. J. McFerran, An inverted crossover resonance aiding laser cooling of ^{171}Yb , J. Opt. Soc. Am. B **33**, 1278 (2016).
- [184] K. Pandey, A. K. Singh, P. V. K. Kumar, M. V. Suryanarayana, and V. Natarajan, Isotope shifts and hyperfine structure in the 555.8-nm $^1S_0 \rightarrow ^3P_1$ line of Yb, Phys. Rev. A **80**, 022518 (2009).
- [185] W.-G. Jin, T. Horiguchi, M. Wakasugi, T. Hasegawa, and W. Yang, Systematic Study of Isotope Shifts and Hyperfine Structures in Yb I by Atomic-Beam Laser Spectroscopy, J. Phys. Soc. Jpn. **60**, 2896 (1991).
- [186] F. Buchinger, A. Mueller, B. Schinzler, K. Wendt, C. Ekström, W. Klempt, and R. Neugart, Fast-beam laser spectroscopy on metastable atoms applied to neutron-deficient ytterbium isotopes, Nucl. Instruments Methods Phys. Res. **202**, 159 (1982).
- [187] J. H. Broadhurst, M. E. Cage, D. L. Clark, G. W. Greenlees, J. A. R. Griffith, and G. R. Isaak, High resolution measurements of isotope shifts and hyperfine splittings for ytterbium using a CW tunable laser, J. Phys. B Mol. Phys. **7**, L513 (1974).
- [188] G. Wandel, Doppelresonanzexperimente zur Untersuchung der Hyperfeinstruktur des $6s6p\ ^3P_1$ -Zustandes von ^{171}Yb und ^{173}Yb , Zeitschrift für Phys. A Hadron. Nucl. **231**, 434 (1970).
- [189] M. Baumann, H. Liening, and G. Wandel, Die Hyperfeinstruktur des $6s6p\ ^3P_1$ -Zustandes von ^{171}Yb und ^{173}Yb , Zeitschrift für Phys. A Hadron. Nucl. **221**, 245 (1969).
- [190] H. Qiao, C.-Y. Sun, C.-Q. Peng, Q.-C. Qi, C.-C. Zhao, M. Zhou, and X.-Y. Xu, Frequency measurement of $6s6p\ ^3P_{0,2}$ - $6s7s\ ^3S_1$ transitions in ultracold ^{171}Yb atoms referenced to local optical clock, Results Phys. **48**, 106439 (2023).
- [191] A. K. Singh, *Hyperfine Structure-Measurement in Alkali-metal Atoms and Ytterbium Atom*, Ph.D. thesis, Indian Institute of Science, Bengaluru (2014).
- [192] T. Wakui, W.-G. Jin, K. Hasegawa, H. Uematsu, T. Minowa, and H. Katsuragawa, High-Resolution Diode-Laser Spectroscopy of the Rare-Earth Elements, J. Phys. Soc. Jpn. **72**, 2219 (2003).
- [193] J. Maier, C. S. Kischkel, and M. Baumann, Hyperfine structure and isotope shift of some even parity levels in the YbI spectrum, Zeitschrift für Phys. D Atoms Mol. Clust. **21**, 145 (1991).
- [194] C. Zhao, Q. Qi, C. Sun, C. Peng, T. Jin, T. Zhang, S. Lei, Y. Xia, S. Feng, and X. Xu, Absolute frequency measurements of the $6s6p\ ^3P_0$ - $5d6s\ ^3D_1$ transitions in $^{170,171,172,173,174,176}\text{Yb}$ by modulation transfer spectroscopy, Phys. Rev. A **110**, 042816 (2024).
- [195] K. Beloy, J. A. Sherman, N. D. Lemke, N. Hinkley, C. W. Oates, and A. D. Ludlow, Determination of the $5d6s\ ^3D_1$ state lifetime and blackbody-radiation clock shift in Yb, Phys. Rev. A **86**, 051404 (2012).
- [196] M. Baumann, M. Braun, A. Gaiser, and H. Liening, Radiative lifetimes and g_J factors of low-lying even-parity levels in the Yb I spectrum, J. Phys. B Mol. Phys. **18**, L601 (1985).
- [197] H. Qiao, L. Liu, M. Zhou, L. Luo, and X. Xu, Investigation of the $6s6p\ ^3P_2$ - $6s7s\ ^3S_1$ transition of ytterbium atoms with modulation-transfer spectroscopy, Appl. Phys. Lett. **122**, 3 (2023).
- [198] M. Zhou, S. Zhang, L. Luo, and X. Xu, Characterization of ytterbium resonance lines at 649 nm with modulation-

- transfer spectroscopy, *Phys. Rev. A* **101**, 062506 (2020).
- [199] C. Schulz, E. Arnold, W. Borchers, W. Neu, R. Neugart, M. Neuroth, E. W. Otten, M. Scherf, K. Wendt, P. Lievens, Y. A. Kudryavtsev, V. S. Letokhov, V. I. Mishin, and V. V. Petrunin, Resonance ionization spectroscopy on a fast atomic ytterbium beam, *J. Phys. B Mol. Opt. Phys.* **24**, 4831 (1991).
- [200] S. Utreja, P. Roy, H. Rathore, S. Choudhury, M. Das, and S. Panja, Cross Beam Saturated Absorption Spectroscopy: A novel technique for optimization of power broadening, *Opt. Commun.* **585**, 131870 (2025).
- [201] M. Johanning, A. Braun, D. Eiteneuer, C. Paape, C. Balzer, W. Neuhauser, and C. Wunderlich, Resonance enhanced isotope-selective photoionization of YbI for ion trap loading (2010), arXiv:0712.0969.
- [202] J. S. Ross, Isotope Shift in $\lambda 5556 \text{ \AA}$ of Ytterbium I, *J. Opt. Soc. Am.* **53**, 299 (1963).
- [203] C. Clivati, G. Cappellini, L. F. Livi, F. Poggiali, M. S. de Cumis, M. Mancini, G. Pagano, M. Frittelli, A. Mura, G. A. Costanzo, F. Levi, D. Calonico, L. Fallani, J. Catani, and M. Inguscio, Measuring absolute frequencies beyond the GPS limit via long-haul optical frequency dissemination, *Opt. Express* **24**, 11865 (2016).
- [204] A. Muzi Falconi, R. Panza, S. Sbernadori, R. Forti, R. Klemt, O. Abdel Karim, M. Marinelli, and F. Scazza, Microsecond-Scale High-Survival and Number-Resolved Detection of Ytterbium Atom Arrays, *Phys. Rev. Lett.* **135**, 203402 (2025).
- [205] W. F. McGrew, *An Ytterbium Optical Lattice Clock with Eighteen Digits of Uncertainty, Instability, and Reproducibility*, Ph.D. thesis, University of Colorado (2020).
- [206] M. A. Norcia, W. B. Cairncross, K. Barnes, P. Battaglini, A. Brown, M. O. Brown, K. Cassella, C.-A. Chen, R. Coxe, D. Crow, J. Epstein, C. Griger, A. M. W. Jones, H. Kim, J. M. Kindem, J. King, S. S. Kondov, K. Kotru, J. Lauigan, M. Li, M. Lu, E. Megidish, J. Marjanovic, M. McDonald, T. Mittiga, J. A. Muniz, S. Narayanaswami, C. Nishiguchi, R. Notermans, T. Paule, K. A. Pawlak, L. S. Peng, A. Ryou, A. Smull, D. Stack, M. Stone, A. Sucich, M. Urbanek, R. J. M. van de Veerndonk, Z. Vendeiro, T. Wilkason, T.-Y. Wu, X. Xie, X. Zhang, and B. J. Bloom, Midcircuit Qubit Measurement and Rearrangement in a ^{171}Yb Atomic Array, *Phys. Rev. X* **13**, 041034 (2023).
- [207] J. W. Lis, A. Senoo, W. F. McGrew, F. Rönchen, A. Jenkins, and A. M. Kaufman, Midcircuit Operations Using the omg Architecture in Neutral Atom Arrays, *Phys. Rev. X* **13**, 041035 (2023).
- [208] M. A. Norcia, H. Kim, W. B. Cairncross, M. Stone, A. Ryou, M. Jaffe, M. O. Brown, K. Barnes, P. Battaglini, T. C. Bohdanowicz, A. Brown, K. Cassella, C.-A. Chen, R. Coxe, D. Crow, J. Epstein, C. Griger, E. Halperin, F. Hummel, A. M. W. Jones, J. M. Kindem, J. King, K. Kotru, J. Lauigan, M. Li, M. Lu, E. Megidish, J. Marjanovic, M. McDonald, T. Mittiga, J. A. Muniz, S. Narayanaswami, C. Nishiguchi, T. Paule, K. A. Pawlak, L. S. Peng, K. L. Pudenz, D. Rodríguez Pérez, A. Smull, D. Stack, M. Urbanek, R. J. M. van de Veerndonk, Z. Vendeiro, L. Wadleigh, T. Wilkason, T.-Y. Wu, X. Xie, E. Zalys-Geller, X. Zhang, and B. J. Bloom, Iterative Assembly of ^{171}Yb Atom Arrays with Cavity-Enhanced Optical Lattices, *PRX Quantum* **5**, 030316 (2024).
- [209] T. A. Zheng, Y. A. Yang, M. S. Safronova, U. I. Safronova, Z. X. Xiong, T. Xia, and Z. T. Lu, Magic wavelengths of the Yb ($6s^2\ ^1S_0$ - $6s6p\ ^3P_1$) intercombination transition, *Phys. Rev. A* **102**, 4 (2020).
- [210] Y. Takasu, K. Komori, K. Honda, M. Kumakura, T. Yabuzaki, and Y. Takahashi, Photoassociation Spectroscopy of Laser-Cooled Ytterbium Atoms, *Phys. Rev. Lett.* **93**, 123202 (2004).
- [211] T. Andersen, O. Poulsen, P. S. Ramanujam, and A. P. Petkov, Lifetimes of some excited states in the rare earths: La ii, Ce ii, Pr ii, Nd ii, Sm ii, Yb i, Yb ii, and Lu ii, *Sol. Phys.* **44**, 257 (1975).
- [212] M. Baumann and G. Wandel, Lifetimes of the excited states ($6s6p$) 1P_1 and ($6s6p$) 3P_1 of ytterbium, *Phys. Lett.* **22**, 283 (1966).
- [213] J. L. Siegel, W. F. McGrew, Y. S. Hassan, C.-C. Chen, K. Bely, T. Grogan, X. Zhang, and A. D. Ludlow, Excited-Band Coherent Delocalization for Improved Optical Lattice Clock Performance, *Phys. Rev. Lett.* **132**, 133201 (2024).
- [214] C.-Y. Xu, J. Singh, J. C. Zappala, K. G. Bailey, M. R. Dietrich, J. P. Greene, W. Jiang, N. D. Lemke, Z.-T. Lu, P. Mueller, and T. P. O'Connor, Measurement of the Hyperfine Quenching Rate of the Clock Transition in ^{171}Yb , *Phys. Rev. Lett.* **113**, 033003 (2014).
- [215] J. E. Golub, Y. S. Bai, and T. W. Mossberg, Radiative and dynamical properties of homogeneously prepared atomic samples, *Phys. Rev. A* **37**, 119 (1988).
- [216] M. Gustavsson, H. Lundberg, L. Nilsson, and S. Svanberg, Lifetime measurements for excited states of rare-earth atoms using pulse modulation of a cw dye-laser beam, *J. Opt. Soc. Am.* **69**, 984 (1979).
- [217] W. Gornik, D. Kaiser, W. Lange, J. Luther, and H.-H. Schulz, Quantum beats under pulsed dye laser excitation, *Opt. Commun.* **6**, 327 (1972).
- [218] B. Budick and J. Snir, Hyperfine-Structure Anomalies of Stable Ytterbium Isotopes, *Phys. Rev. A* **1**, 545 (1970).